Mechanical Systems and Signal Processing 240 (2025) 113317

Contents lists available at ScienceDirect

Mechanical Systems and Signal Processing

journal homepage: www.elsevier.com/locate/ymssp

Full length article

# Enhanced delayed resonator for complete single- and multiple-frequency vibration suppression: A hybrid feedforward-feedback control approach

Yifan Liu [a], Bo Yan [b], Jianwang Shao [c], Li Cheng [a,*]

[a] Department of Mechanical Engineering, The Hong Kong Polytechnic University, Hong Kong, China
[b] School of Mechanical Engineering, Zhejiang Sci-Tech University, Hangzhou, China
[c] School of Automotive Studies, Tongji University, Shanghai, China

ARTICLE INFO

Communicated by M. Krack

*Keywords:*
Active vibration control
Delayed resonator
Dynamical control
Feedforward and feedback

ABSTRACT

Delayed resonator (DR) is an active vibration absorber capable of achieving complete vibration suppression at a specific frequency by distinctively incorporating appropriate time delays into the control loop. Existing works drive the DR mainly following the absorber-based feedback control laws. Alternatively, we here propose a hybrid control law that integrates both feedforward and feedback control, in which the feedforward control is based on excitation and the feedback one is based on the states of the primary structure instead of the absorber. A resulting key benefit is that system stability analysis can be significantly simplified thanks to the decoupling between the control parameters to be tuned and the characteristic equation. In addition to this, enhanced control performance over classical DRs is achieved in both cases of single- and multiple-frequency vibration suppression. Results show that the hybrid control law can extend the operable frequency band, expedite setting the transient process, and extend the antiresonance valley to suppress residual vibrations in steady states. Particularly, the alleviated stability issues in the multiple-frequency case allow the hybrid control law to fully leverage the strength of the delayed control in raising system order so that a single-mass absorber can yield multiple zero antiresonance points at multiple given frequencies. This work establishes a basic design and analysis framework for applying feedforward control to the DR and combining it with feedback control strategies to maximize control performance.

## 1. Introduction

Vibration absorbers suppress vibrations by canceling forces on primary structures. To perfect force cancellation for complete vibration suppression independent of absorber structural parameters, Olgac and Holm-Hansen [1] proposed a concept of delayed resonator (DR) by driving the absorber using the delayed control, which generated current active forces as per passive system states. Compared to the delay-free control laws (e.g., PD control [2]), the use of delay as a control parameter can directly alter the phase of the active force without increasing control terms while maintaining system linearity. As such, displacement [1], velocity [3], and acceleration [4] can all be individually used as feedback states to simplify sensor deployments and enhance robustness.

The research on DR has yielded fruitful results. Focusing on the past decade, Sun et al. [5] and Xu et al. [6] identified the loop delay, which was then increased to enhance vibration reduction. Pilbauer et al. [7] and Kučera et al. [8] adopted distributed-delayed control laws to reduce measurement noise by generating active forces based on the sum of all the absorber states within

* Corresponding author.
*E-mail address:* li.cheng@polyu.edu.hk (L. Cheng).

https://doi.org/10.1016/j.ymssp.2025.113317
Received 17 March 2025; Received in revised form 24 June 2025; Accepted 2 September 2025

a past time interval. Liu et al. [9] further opined that ignoring the loop delay when using the distributed control, even though it is small, can possibly result in no vibration suppression. To reduce the effects of the mismatch between the detected and in-situ vibration frequencies, Pilbauer et al. [10] extended the antiresonance valley by properly assigning distributed delays, see also [11] for achieving the task by assigning double imaginary roots to the DR subsystem. Eris et al. [12] injected an additional non-delayed control term and expedited the transient process by optimizing characteristic spectra. Vyhlídal et al. [13] compared the tuning mechanisms of control parameters when incorporating different absorber states. Cai et al. [14,15] further unified such tuning mechanisms using a fractional-order operator. Zhang et al. [16] integrated the DR into a seat suspension to cope with both harmonic and random excitations, see also [17]. Furthermore, the nonlinear effects of stiffness and friction on DR tuning were investigated in [18–20]. The DR was also generalized to multiple-degree-of-freedom (MDOF) structures for multiple-dimensional vibration control in robotic applications [21–23] and to achieve non-collected vibration suppression [24–26]. In addition to complete vibration suppression, delayed control has also been widely used to enhance vibration reduction [27–33].

We notice from the existing works that stability analysis always accounts for a significant portion of the efforts when determining the operable frequency band to achieve complete vibration suppression since control parameters affect system stability. However, the existing delays lead to an infinite-dimensional system with infinite characteristic roots [34], which prevents a complete stability analysis as the control task becomes more complex, thus requiring advanced numerical tools to perform spectral checks at each frequency where vibration suppression is to be achieved, e.g., [10,23,26]. This can obviously hamper the application of DR. It should also be noted that feedback control, which has been used since the invention of DR, is the root of the stability problem given that instability or destabilization is essentially an inappropriate interaction between system input (active forces) and output (responses). Motivated by this, we alternatively consider feedforward control since feedforward control based on disturbances (i.e., excitations in a vibrating system) as input is independent of system output and thus does not affect system stability.

In fact, the feedforward control has been used to enhance vibration suppression. For instance, Zhu et al. [35] proposed an adaptive feedforward controller to settle a piezoelectric cantilever beam under unknown excitation frequencies. Matsui et al. [36] used feedforward control to achieve anti-sway transport of a suspended load in a crane system. Beijen et al. [37] minimized the measurement noises and improved vibration isolation efficacy using the feedforward control. In the meantime, feedforward control is often combined with feedback control to maximize the control performance. In this case, Yan et al. [38] improved a nonlinear vibration isolator by reducing the peak transmissibility while maintaining the isolation efficacy. Lang et al. [39] reduced vibrations of a helicopter fuselage using partial system states. Zhou et al. [40] eliminated nonlinear hysteretic or creep issues of a camber wing. More discussions on the benefits of combining feedback and feedforward can also be referred to [41–44].

Since the purpose of using feedforward control is to simplify the stability analysis in the classical feedback-controlled cases, it may seem paradoxical if we also additionally introduce feedback control to drive the DR for combined benefits. To understand this, we further point out that the classical feedback-controlled DRs are based on absorber states. Differently, we here use the states of the primary structure for feedback control, and we activate the resulting feedback force only when the primary is not fully settled. That is, the feedforward force yields complete vibration suppression in steady states where the feedback force takes no effect. In this way, the feedback force does not affect the tuning of the control parameters governing the feedforward force for complete vibration suppression. On the other hand, such feedforward control parameters do not affect stability that depends only on feedback force. Thus, the tuning mechanisms of feedforward and feedback forces can be completely decoupled from each other for simplification, forming the basis of proposing a hybrid feedforward (based on excitation) and feedback (based on the primary) control law. This also further simplifies our recent works [45,46], where the control logic is combined with the states of the primary and absorber.

We focus on two tasks to show the benefits of the hybrid control law: (1). The commonly studied problem of single-frequency vibration suppression, and (2). The multiple-frequency case by still using a single-mass absorber, which is a unique strength of the delayed control thanks to the raised system order [47,48]. In both cases, we show how the severe stability issues of the classical DRs limit the operable frequency band and how to address or avoid them by the proposed hybrid control law. Besides, the feature that feedback forces are activated when the primary structure is not settled makes it possible to enhance transient performances and reduce residual vibrations in steady states. Overall, twofold comparisons are conducted: (1). Comparisons with the classical absorber-based DRs, and (2) between the cases where the feedforward control is and is not combined with the feedback one, to justify the benefits and design rules of the 'hybrid' control mode.

The paper is structured as follows. Section 2 establishes the system model. Section 3 proposes the hybrid control law with the motivation and necessity of the active control highlighted. Stability issues are addressed in Section 4. Sections 5 and 6 discuss the single- and multiple-frequency vibrations, respectively. Numerical and experimental verifications are conducted in Section 7. Conclusions are drawn in Section 8. Italic symbols without the bar superscript '$\overline{\square}$' are dimensionless throughout the text.

## 2. System model and governing equations

A common operating mode of the DR is shown in Fig. 1(a), in which an actuation force $\bar{u}$ based on actively delayed system states is injected into the vibration absorber. By properly tuning $\bar{u}$, the DR aims to completely settle the primary structure that is harmonically excited by $\bar{f}_e$. Once achieved, the resulting settled system acts like Fig. 1(b), i.e., the primary structure is fixed and only the absorber oscillates to neutralize or cancel the effect of $\bar{f}_e \neq 0$, yielding the so-called complete vibration suppression.

As marked in Fig. 1, structural dynamics between each two among the primary structure, absorber, and slides are modeled by a pair of spring and damper, in which the stiffness between the absorber and slides is omitted due to its small values compared with the absorber support stiffness denoted as $\bar{k}_a$. Dynamics of the primary structure and the absorber are then governed by

$$\begin{cases} \bar{m}_a\ddot{\bar{x}}_a + \bar{c}_g\dot{\bar{x}}_a + \bar{c}_a\left(\dot{\bar{x}}_a - \dot{\bar{x}}_p\right) + \bar{k}_a\left(\bar{x}_a - \bar{x}_p\right) = \bar{u}, \\ \bar{m}_p\ddot{\bar{x}}_p + \bar{c}_p\dot{\bar{x}}_p + \bar{k}_p\bar{x}_p + \bar{c}_a\left(\dot{\bar{x}}_p - \dot{\bar{x}}_a\right) + \bar{k}_a\left(\bar{x}_p - \bar{x}_a\right) = \bar{f}_e - \bar{u}, \end{cases} \tag{1}$$

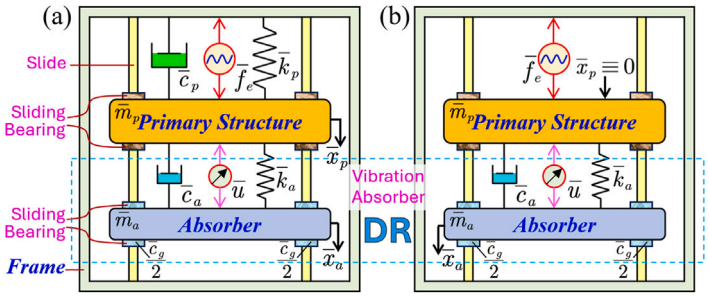


**Fig. 1.** (a). An operating mode of DR to settle a primary structure. (b). Reduced model when the primary is completely settled.

where $\bar{m}_{(\cdot)}$, $\bar{c}_{(\cdot)}$, $\bar{k}_{(\cdot)}$, and $\bar{x}_{(\cdot)}$ represent mass, damping, stiffness, and absolute displacement, respectively; $\bar{x}_{(\cdot)}$, $\bar{u}$, and $\bar{f}_e$ are functions of the time $\bar{t}$. Introducing the following variable transformations

$$\begin{aligned}&\bar{\omega}_p=\sqrt{\bar{k}_p/\bar{m}_p},\bar{\omega}_a=\sqrt{\bar{k}_a/\bar{m}_a},\zeta_p=\frac{\bar{c}_p}{2\bar{m}_p\bar{\omega}_p},\zeta_a=\frac{\bar{c}_a}{2\bar{m}_a\bar{\omega}_a},\zeta_g=\frac{\bar{c}_g}{2\bar{m}_a\bar{\omega}_a},\\&\mu=\frac{\bar{m}_a}{\bar{m}_p},\upsilon=\frac{\bar{\omega}_a}{\bar{\omega}_p},x_a=\frac{\bar{x}_a}{\bar{l}},x_p=\frac{\bar{x}_p}{\bar{l}},t=\bar{t}\bar{\omega}_p,f_e=\frac{\bar{f}_e}{\bar{k}_p\bar{l}},u=\frac{\bar{u}}{\bar{k}_p\bar{l}},\end{aligned}\tag{2}$$

in which $\bar{l}$ denotes the unit length, Eq. (1) can be reshaped into the dimensionless form as

$$\begin{cases}\mu\left[\ddot{x}_a+2\zeta_g\upsilon\dot{x}_a+2\zeta_a\upsilon\left(\dot{x}_a-\dot{x}_p\right)+\upsilon^2\left(x_a-x_p\right)\right]=u,\\ \ddot{x}_p+2\zeta_p\dot{x}_p+x_p+\mu\left[2\zeta_a\upsilon\left(\dot{x}_p-\dot{x}_a\right)+\upsilon^2\left(x_p-x_a\right)\right]=f_e-u.\end{cases}\tag{3}$$

The desired complete vibration suppression is to achieve $\left|x_p\right|=0$ when $\left|f_e\right|\neq 0$ by properly constructing the form of the controlled active actuation force $u$, and accordingly, tuning the control parameters.

**Remark 1.** Like most studies on DRs, the circuit dynamics within the actuator for generating $u$ are not considered. This agrees with our physical implementation of $u$ by directly applying the driving current in the coil of a voice coil motor, as to be further introduced in Section 7.1. If the motor driving is based on voltage, then the effects of the coil inductance and resistance need to be considered for correcting the coil current [2,38,49]. Note that in both implementation methods, the force output $u$ is linearly proportional to the coil current. From this perspective, directly driving $u$ via the current can simplify the analysis given also the complexity of the time-delayed system itself. In addition to the extensive studies on DRs, one can also refer to [50–52] for the force control of voice coil motors based on the direct-current-driven methods. ■

## 3. Proposition of the hybrid control law

To facilitate comparisons, we start with reviewing the most commonly considered absorber displacement-based control logic

$$u_a\left(t,g_a^{[i]},\tau_a^{[i]}\right)=\sum_{i=1}^{N_a}g_a^{[i]}x_a\left(t-\tau_a^{[i]}\right),\tag{4}$$

where $N_a\in\mathbb{Z}^+$, $g_a^{[i]}$ is the gain, and $\tau_a^{[i]}$ is the time delay. The introduction of the time delay $\tau_a^{[i]}$ renders a single control term with two manipulatable parameters without affecting system linearity, in addition to modeling the inevitable loop delay in real applications. Note that $u_a$ is a feedback control law based on system responses (output).

### 3.1. System responses with a general actuation force $u$

Revisiting Fig. 1(a), the excitation $f_e$ independent of system states $\left(x_a,x_p\right)$ can be seen as a disturbance, and the coupled system contains a single input ($u$) and two outputs $\left(x_a,x_p\right)$. To enhance performance, we generalize the classical control law $u_a$ in (4) by incorporating all three states $\left(f_e,x_a,x_p\right)$ into the generation of the active force $u$ by considering

$$u\left(u_a,u_f,u_p\right)=u_a\left(t\right)+u_f\left(t\right)+u_p\left(t\right),\tag{5}$$

where $u_a$, $u_p$, and $u_f$ can be taken as the general forms of linear control terms related to $x_a$, $x_p$, and $f_e$ (including their derivatives), respectively. Particularly, $u_f$ based on the disturbance $f_e$ is a feedforward force. The Laplace transform of $u$ is

$$U\left(U_a,U_p,U_f\right)=U_a\left(s\right)X_a+U_p\left(s\right)X_p+U_f\left(s\right)F_e,\tag{6}$$

where $s$ is the Laplace variable, $X_a = \mathscr{L}(x_a)$, $X_p = \mathscr{L}(x_p)$, and $F_e = \mathscr{L}(f_e)$, with $\mathscr{L}(\cdot)$ denoting Laplace transform operation, and accordingly, $U_a(s) = \mathscr{L}(u_a)/X_a$, $U_p(s) = \mathscr{L}(u_p)/X_p$, and $U_f(s) = \mathscr{L}(f_e)/F_e$. Substituting (6) into (3), the governing equations in the Laplace domain can be cast into a matrix form of

$$\mathbf{Z}(s, U_a, U_p)\begin{bmatrix} X_a \\ X_p \end{bmatrix} = \begin{bmatrix} U_f(s) F_e \\ (1 - U_f(s)) F_e \end{bmatrix}, \tag{7}$$

where $\mathbf{Z}$ is the impedance matrix and is defined as

$$\mathbf{Z}(s, U_a, U_p) = \begin{bmatrix} A(s, U_a) & B(s, U_p) \\ C(s, U_a) & D(s, U_p) \end{bmatrix}, \tag{8}$$

in which

$$\begin{cases} A(s, U_a) = \mu\left(s^2 + 2(\zeta_a + \zeta_g) v s + v^2\right) - U_a(s), \\ B(s, U_p) = -\mu v (2\zeta_a s + v) - U_p(s), \\ C(s, U_a) = -\mu v (2\zeta_a s + v) + U_a(s), \\ D(s, U_p) = s^2 + 2\zeta_p s + 1 + \mu v (2\zeta_a s + v) + U_p(s). \end{cases} \tag{9}$$

One can then obtain the transfer function from $f_e$ to $x_p$,

$$G_{fe \to xp}(s, U_a, U_p, U_f) = \frac{X_p}{F_e} = U_f(s)\mathbf{Z}^{-1}_{(2,1)}(s, U_a, U_p) + \left[1 - U_f(s)\right]\mathbf{Z}^{-1}_{(2,2)}(s, U_a, U_p), \tag{10}$$

where $\mathbf{Z}^{-1}_{(2,1)}$ and $\mathbf{Z}^{-1}_{(2,2)}$ represent the $(2,1)$ and $(2,2)$ elements of the matrix $\mathbf{Z}^{-1}$, respectively. We next write the transfer function (10) into a more concise form as

$$G_{fe \to xp}(s, U_a, U_p, U_f) = \frac{N(s, U_a, U_f)}{\left|\mathbf{Z}(s, U_a, U_p)\right|}, \tag{11}$$

where $|\cdot|$ means calculating the determinant, and $N$ is a function of $(s, U_a, U_f)$, i.e.,

$$N(s, U_a, U_f) = -U_f(s) C(s, U_a) + \left[1 - U_f(s)\right] A(s, U_a). \tag{12}$$

Hence, the active force $u$ affects the responses of the primary by injecting $(U_a, U_p, U_f)$ terms into the transfer function (10).

### 3.2. Motivation for the hybrid multiple-delayed control law

The complete vibration suppression $|x_p| \equiv 0$ necessitates an ideal zero antiresonance point of the primary structure at a given frequency, say $\omega_t \in \mathbb{R}^+$ in the dimensionless form. To this end, we let $G(s = j\omega_t) = 0$, which is equivalent to

$$N(s = j\omega_t, U_a, U_f) = 0, \tag{13}$$

where $j = \sqrt{-1}$. On the other hand, the active force $u$ makes sense only if the coupled system is stable, which requires that the spectrum of the characteristic equation

$$CE(s, U_a, U_p) = \left|\mathbf{Z}(s, U_a, U_p)\right| = 0 \tag{14}$$

all lies on the left half of the complex plane. Eqs. (13) and (14) signify two basic design rules of $u$, regardless of control laws.

From the form of (14), the feedforward control force $u_f$ signified by $U_f$ does not appear in the characteristic equation and thus does not affect system stability. This is expected since $f_e$ which $u_f$ depends on is independent of system states. On the other hand, the feedback force $u_p$ related to the primary structure does not appear in (13), thus posing no effects on the tuning mechanisms of the control parameters governing $(U_a, U_f)$ for complete vibration suppression. Considering that $U_a$ appears in both (13) and (14), one can adopt a control law in the form of

$$u_h(u_f, u_p) = u_f(t) + u_p(t), \tag{15}$$

which *excludes* the feedback force $u_a$ related to absorber states. By adopting (15), we have $U_a = 0$ so that the tuning process for complete vibration suppression only involves $U_f$ as per (13) and is decoupled from system stability which is now only tied to $U_p$ as per (14). From this perspective, the operable frequency band for complete vibration suppression, which is known to be severely limited by stability issues when absorber states are involved in $u$ [13,14,45,48], can be extended. Note that the system is always stable when adopting (15) with $u_p = 0$ since Eq. (14) with $U_a = U_p = 0$ reduces to the passive case.

### 3.3. Necessity of the active vibration absorber

Given that the information of the excitation $f_e$ is required in $u_f$, the necessity of the active vibration absorber may be questioned since it seems that one can now directly apply a counter force $-f_e$ on the primary to neutralize $f_e$ for complete vibration suppression

$\left|x_p\right| = 0$. To explain the necessity, we substitute the condition $\left|x_p\right| = 0$ into (3), yielding

$$\begin{cases} \mu\left(\ddot{x}_a + 2\zeta_g \upsilon \dot{x}_a + 2\zeta_a \upsilon \dot{x}_a + \upsilon^2 x_a\right) = u_a + u_f + u_p, \\ -\mu\left(2\zeta_a \upsilon \dot{x}_a + \upsilon^2 x_a\right) = f_e - \left(u_a + u_f + u_p\right), \end{cases} \tag{16}$$

where we let $u_p = 0$ when $\left|x_p\right| = 0$ and have $u_a \equiv 0$ when adopting (15). Summing the two equations in (16) gives

$$\mu\left(\ddot{x}_a + 2\zeta_g \upsilon \dot{x}_a\right) = f_e. \tag{17}$$

Combining Eq. (17) and the first equation of (16), one can obtain the transfer function from $f_e$ to $u_f$,

$$G_{fe\to uf}(s) = \frac{U_f}{F_e} = \frac{s^2 + 2\left(\zeta_g + \zeta_a\right)\upsilon s + \upsilon^2}{s^2 + 2\zeta_g \upsilon s}. \tag{18}$$

The amplitude of (18) is

$$G_{fe\to uf}(\omega) = \frac{\left|u_f\right|}{\left|f_e\right|} = \sqrt{\frac{\left(\upsilon^2 - \omega^2\right)^2 + 4\left(\zeta_g + \zeta_a\right)^2 \upsilon^2 \omega^2}{\omega^4 + 4\zeta_g^2 \upsilon^2 \omega^2}} = \sqrt{1 + \upsilon^2 \vartheta(\omega)}, \tag{19}$$

where $\omega \in \mathbb{R}^+$ is the dimensionless excitation frequency, and

$$\vartheta(\omega) = 2\left(2\zeta_a^2 + 4\zeta_g\zeta_a - 1\right)\omega^2 + \upsilon^2. \tag{20}$$

Note that $G_{fe\to uf}(\omega) < 1$ means that the active force combined with a vibration absorber to achieve $\left|x_p\right| = 0$ is smaller than the one directly applied on the primary to neutralize $f_e$. To achieve this, we require $\vartheta < 0$. Given that $\zeta_g, \zeta_a \ll 1$, one needs

$$\omega^2 > \frac{\upsilon^2}{2\left(1 - 2\zeta_a^2 - 4\zeta_g\zeta_a\right)}. \tag{21}$$

Hence, by properly designing $\left(\upsilon, \zeta_a, \zeta_g\right)$ related to the absorber structure, the solution of active vibration absorber can achieve

$$\left|u_f\right| < \left|f_e\right| \tag{22}$$

within a sufficiently broad frequency band. This favorably reduces the power and size requirements of the actuator. On the other hand, when the primary structure is far from the frame or base making directly apply forces to neutralize $f_e$ difficult, which is common in engineering practice, the absorber substructure can provide mounting space for the actuator to generate $u_f$.

In this work, we consider an example system with

$$\begin{aligned} &\mu = 0.5285, \upsilon = 0.9862, \zeta_a = 0.1097, \zeta_g = 0.051, \zeta_p = 0.0665, \\ &\bar{\omega}_a = 38.42 \text{ rad/s}\,(6.11 \text{ Hz}), \bar{\omega}_p = 38.96 \text{ rad/s}\,(6.2 \text{ Hz}). \end{aligned} \tag{23}$$

The corresponding experimental setup is to be introduced in Section 7. According to (21), we can achieve (22) when $\omega > 0.714$ or $\bar{\omega} = \omega\bar{\omega}_p > 4.428$ Hz. Note that Eq. (19) monotonically decreases with $\omega$, and $G_{fe\to uf}(\omega) = 0.63 \ll 1$ when $\bar{\omega} = 5$ Hz.

### 3.4. Specification of the hybrid multiple-delayed control law

To demonstrate the strength of the hybrid multiple-delayed control law (15), we specify $u_h$ based on $\left(f_e, x_p\right)$ following

$$u_h :\Rightarrow u_{FP}\left(f_e, x_p\right) = \underbrace{\sum_{i=1}^{N_f} g_f^{[i]} f_e\left(t - \tau_f^{[i]}\right)}_{u_f} + \underbrace{g_p x_p\left(t - \tau_p\right)}_{u_p}, \tag{24}$$

where $N_f \in \mathbb{Z}^+$, $\left(g_f^{[i]}, g_p\right)$ are gain parameters, and $\left(\tau_f^{[i]}, \tau_p\right)$ are manipulable delay parameters similar to $\tau_a^{[i]}$ of the classical control law $u_a$ in (4) to seek enhanced performance by manipulating the state phase. Note that $u_{FP}$ is a hybrid multiple-delayed control law consisting of both delayed feedforward and feedback states, as graphically illustrated in Fig. 2. Particularly, to minimize the number of control terms for robustness and simplification, only one feedback control term $u_p(t) = g_p x_p\left(t - \tau_p\right)$ is used to show how to manipulate the interplay between the feedforward and feedback forces for better performance, given also that the form of $u_p$ does not affect the tuning of $u_f$ for complete vibration suppression, see Section 3.2. Besides, $N_f = 1$ and $N_f > 1$ correspond to single- and multiple-frequency vibration suppressions, respectively, as to be further introduced.

Next, the DR actuated with the classical control law $u_a$ and the hybrid one $u_{FP}$ is called A-DR and FP-DR, respectively. The reduced case of FP-DR with $g_p = 0$, which corresponds to pure feedforward control, is called F-DR. The benefits of the FP-DR over F-DR and A-DR are sought in two aspects: (1). Single-frequency vibration suppression, followed by (2). The multiple-frequency case. Before such discussions, stability issues governed by (14) of the FP-DR are addressed.

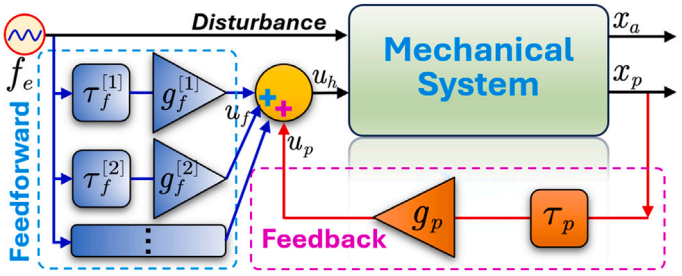


**Fig. 2.** Proposed hybrid multiple-delayed control logic ($u_{FP}$) with both delayed feedforward ($u_f$) and feedback ($u_p$) states.

## 4. System stability analysis on FP-DR for stable pairs of $(g_p, \tau_p)$

Since the characteristic Eq. (14) in the FP-DR case is only related to $U_p$, the operable pairs of $(g_p, \tau_p)$ rendering a stable system hold whether complete vibration suppression is achieved at single or multiple frequencies, as to be determined next.

### 4.1. Stability boundaries

When adopting the FP-DR driven by $u_{FP}$ in (24), we according to (6) have

$$\begin{cases} U_a(s) = 0, U_p(s) = g_p e^{-\tau_p s}, \\ U_f(s) = \sum_{i=1}^{N_f} g_f^{[i]} e^{-\tau_f^{[1]} s}. \end{cases} \tag{25}$$

Substituting $(U_a, U_p)$ in (25) into (14) and combining the terms related to $g_p e^{-\tau_p s}$ of the resulting equation yield

$$CE_h(s, g_p, \tau_p) = \alpha(s) g_p e^{-\tau_p s} + \beta(s) = 0, \tag{26}$$

where $(\alpha, \beta)$ are two complex polynomials in the forms of

$$\begin{cases} \alpha(s) = \mu\left(s^2 + 2\zeta_g \upsilon s\right), \\ \beta(s) = \mu\left(s^2 + 2\left(\zeta_a + \zeta_g\right)\upsilon s + \upsilon^2\right)\left[s^2 + 2\zeta_p s + 1 + \mu\upsilon\left(2\zeta_a s + \upsilon\right)\right] - \mu^2\upsilon^2\left(2\zeta_a s + \upsilon\right)^2. \end{cases} \tag{27}$$

Linear systems lose stability at the critical moment when the rightmost pair of characteristic roots crosses the imaginary axis from the left to the right. Hence, substituting $s = j\omega_c, \omega_c \in \mathbb{R}^+$ into (26) leads to

$$g_p e^{-j\tau_p \omega_c} = -\frac{\beta(j\omega_c)}{\alpha(j\omega_c)} = \gamma_R(\omega_c) + j\gamma_I(\omega_c), \tag{28}$$

where the subscript $(\cdot)_c$ means 'critical', and $(\gamma_R, \gamma_I) \in \mathbb{R}^{2+}$ denote the expansion. Balancing the real and imaginary parts of (28), the pairs of $(g_p, \tau_p)$ yielding at least one pair of imaginary roots $s = \pm j\omega_c$ can be obtained as

$$\begin{cases} g_{p,c}(\omega_c) = \rho_c \sqrt{\gamma_R^2(\omega_c) + \gamma_I^2(\omega_c)}, \\ \tau_{p,c}(\omega_c) = \frac{1}{\omega_t}\left[\mathrm{a}\tan\left(\frac{-\gamma_I(\omega_c)}{\gamma_R(\omega_c)}\right) + 2\pi(q-1) + \frac{|\rho_c| - \rho_c}{2}\pi\right], \end{cases} \tag{29}$$

where $\rho_c = \pm 1$, and $q = 1, 2, \ldots$ stem from the periodicity of $e^{-j\tau_{p,c}\omega_c}$. By exhaustively sweeping $\omega_c$, the resulting critical pairs of $(g_{p,c}, \tau_{p,c})$ signify all positions where destabilization can occur, and thus the curves constituted by $(g_{p,c}, \tau_{p,c})$ are called stability boundaries. The stability analysis based on stability boundaries is known as the D-subdivision method [53].

### 4.2. Stability map

The stability boundaries $(g_{p,c}, \tau_{p,c})$ resulting from (29) for the coupled system (23) are shown as the solid curves in Fig. 3, which divide the $(g_p, \tau_p)$ plane into infinite parametric pockets. Parameter pairs $(g_p, \tau_p)$ within each pocket do not alter stability since no boundary crossings occur. To determine the stable regions for operable pairs of $(g_p, \tau_p)$, we start with the pocket covering $g_p = 0$, which is the F-DR case and is always stable since the characteristic Eq. (26) with $g_p = 0$ is reduced to the passive case, see also Section 3.2. Then, the stability of rest pockets can be checked by the required boundary crossings from the stable one via the root tendency (RT) [54] defined as

$$RT = \mathrm{sgn}\left[\mathrm{Re}\left(\left.\frac{ds}{d\lambda}\right|_{\substack{s=j\omega_c \\ \lambda=\lambda_c}}\right)\right], \tag{30}$$

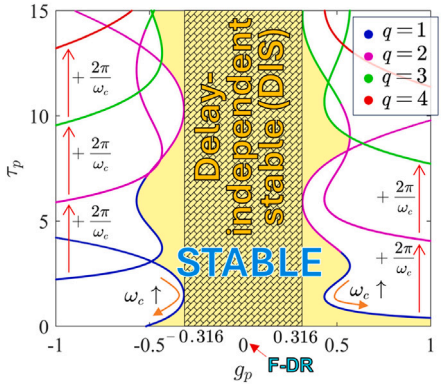


**Fig. 3.** Stability map regarding Eq. (26) for the system (23). Colored region is stable. Shaded region is delay-independent stable.

where $\lambda \in [g_p, \tau_p]$ corresponds to the variable that crosses stability boundaries. Clearly, the crossings with $RT = +1$ and $RT = -1$ shift the imaginary roots $s = \pm j\omega_c$ rightward and leftward, respectively. By counting the number of unstable roots based on RT, the stable regions can be determined, as colored in Fig. 3.

### 4.3. Delay-independent stability

The stable region shown in Fig. 3 signifies the operable $(g_p, \tau_p)$ pairs of the FP-DR regardless of the feedforward force $u_f$ governed by $\left(g_f^{[i]}, \tau_f^{[i]}\right)$. Clearly, the delay $\tau_p$ can significantly affect stability. Note that there exists an interval $|g_p| < 0.316$ where the system is stable independent of $\tau_p$, yielding the so-called delay-independent stability (DIS) [55–57].

The mechanism of DIS is to ensure that no boundary crossing occurs when varying $\tau_p$ for a given $g_p$, which requires that $|g_p|$ is smaller than the smallest $|g_{p,c}|$, say $g_{p,c}^{[\min]} \in \mathbb{R}^+$, which agrees with the DIS distribution in Fig. 3. To determine $g_{p,c}^{[\min]}$, we first determine all the grids of $\omega_c$ where $|g_{p,c}|$ exhibits an extremum. According to (28), such $\omega_c$ grids are obtained as

$$\boldsymbol{\omega}_c^{[\mathrm{exm}]} = \left\{ \omega_c \left| \frac{\partial \beta_{abs}(\omega_c)}{\partial \omega_c} \alpha_{abs}(\omega_c) - \frac{\partial \alpha_{abs}(\omega_c)}{\partial \omega_c} \beta_{abs}(\omega_c) = 0 \right. \right\}, \tag{31}$$

where $\beta_{abs} = \left|\beta(j\omega_c)\right|$ and $\alpha_{abs} = \left|\alpha(j\omega_c)\right|$. Then, one can obtain the minimum $g_{p,c}^{[\min]}$ as

$$g_{p,c}^{[\min]} = \min\left\{ g_{p,c}\left(\omega_c^{[\mathrm{exm}]}\right), \forall \omega_c^{[\mathrm{exm}]} \in \boldsymbol{\omega}_c^{[\mathrm{exm}]} \right\}, \tag{32}$$

leading to the DIS condition

$$|g_p| < g_{p,c}^{[\min]}. \tag{33}$$

For the system (23), we have $g_{p,c}^{[\min]} = 0.316$, concurring with Fig. 3. We stress that the determination process of $g_{p,c}^{[\min]}$ based on (31) and (32) is nonconservative since $\boldsymbol{\omega}_c^{[\mathrm{exm}]}$ can be exhaustive thanks to the polynomial forms of $\alpha_{abs}(\omega_c)$ and $\beta_{abs}(\omega_c)$. Selecting $g_p$ following (33) to achieve the DIS can enhance control robustness when the loop delay is large (e.g., hardware delay and delay of numerical filter) and when delay perturbation is non-ignorable. Stability analyses for operable $(g_a, \tau_a)$ of the A-DR in the single-frequency case have been addressed in our previous work [45] and are only spectrally examined next.

## 5. Complete suppression of single-frequency vibrations

In this single-frequency case using the A-DR, FP-DR, or its special case F-DR, we let $g_a^{[i]}, g_f^{[i]} = 0$, for $i \geqslant 2$, to minimize the number of control terms. Accordingly, the tuning mechanisms of $\left(g_f^{[1]}, \tau_f^{[1]}\right)$ for the FP-DR and F-DR and $\left(g_a^{[1]}, \tau_a^{[1]}\right)$ for the A-DR are established, and comparisons are conducted to demonstrate the selection rules of $(g_p, \tau_p)$.

### 5.1. Tuned control parameters for complete vibration suppression

Substituting $U_f$ in (25) with $g_f^{[i]} = 0, i \geqslant 2$ into (13) yields

$$N\left(j\omega_t, g_f^{[1]}, \tau_f^{[1]}\right) = j\mu v\left(2\zeta_a\omega_t + v\right) g_f^{[1]} e^{-j\tau_f^{[1]}\omega_t} + \left(1 - g_f^{[1]} e^{-\tau_f^{[1]}\omega_t}\right)\left[\mu\left(-\omega_t^2 + 2j\left(\zeta_a + \zeta_g\right) v\omega_t + v^2\right)\right] = 0. \tag{34}$$

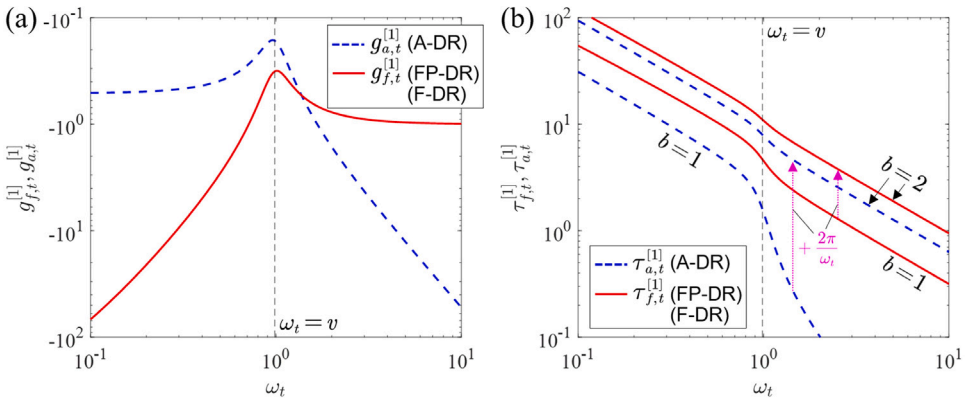


**Fig. 4.** Comparisons of the tuned pairs between the FP-DR (and F-DR) and the A-DR for the coupled system (23), in which $g_a^{[i]}, g_f^{[i]} = 0, i \geqslant 2$. (a). Tuned gain parameters $\left(g_{f,t}^{[1]}, g_{a,t}^{[1]}\right)$ with $(\rho_f < 0, \rho_a < 0)$ versus $\omega_t$. (b). The first two branches of the tuned delays $\left(\tau_{f,t}^{[1]}, \tau_{a,t}^{[1]}\right)$ versus $\omega_t$.

Separating $g_f^{[1]} \exp\left(-j\tau_f^{[1]}\omega_t\right)$ from Eq. (34) and separating the real and imaginary parts of the reminder term arrive at

$$g_f^{[1]} e^{-j\tau_f^{[1]}\omega_t} = \sigma\left(\omega_t\right) + j\varpi\left(\omega_t\right), \tag{35}$$

where $(\sigma, \varpi) \in \mathbb{R}^2$ are parameterized in $\omega_t$, satisfying

$$\sigma\left(\omega_t\right) + j\varpi\left(\omega_t\right) = \frac{v^2 - \omega_t^2 + 2j\left(\zeta_a + \zeta_g\right)v\omega_t}{-\omega_t^2 + 2j\zeta_g v\omega_t}. \tag{36}$$

Note that Eq. (35) corresponds to the transfer function (18) in the frequency domain. Balancing the real and imaginary parts on both sides of (36) leads to the tuned pair of $\left(g_f^{[1]}, \tau_f^{[1]}\right)$ denoted as

$$\begin{cases} g_{f,t}^{[1]}\left(\omega_t\right) = \rho_f \sqrt{\sigma^2\left(\omega_t\right) + \varpi^2\left(\omega_t\right)}, \\ \tau_{f,t}^{[1]}\left(\omega_t\right) = \frac{1}{\omega_t}\left[\operatorname{atan}\left(\frac{-\varpi(\omega_t)}{\sigma(\omega_t)}\right) + 2\pi\left(b-1\right) + \frac{|\rho_f| - \rho_f}{2}\pi\right], \end{cases} \tag{37}$$

where $\rho_f = \pm 1$, and $b \in \mathbb{Z}^+$ similar to $q$ in (29) is called branch number. Note that $\left(g_{f,t}^{[1]}, \tau_{f,t}^{[1]}\right)$ are independent of $\left(g_p, \tau_p\right)$, and they hold for both FP-DR and F-DR. On the other hand, to achieve complete vibration suppression using the A-DR driven by (4) with $g_a^{[i]} = 0, i \geqslant 2$, the tuned pairs of $\left(g_a^{[1]}, \tau_a^{[1]}\right)$ have been obtained in [13] and are rewritten following (2) as

$$\begin{cases} g_{a,t}^{[1]}\left(\omega_t\right) = \rho_a \mu \sqrt{\left(v^2 - \omega_t^2\right)^2 + 4v^2\omega_t^2\left(\zeta_a + \zeta_g\right)^2}, \\ \tau_{a,t}^{[1]}\left(\omega_t\right) = \frac{1}{\omega_t}\left[\operatorname{atan}\left(\frac{-2\left(\zeta_a+\zeta_g\right)v\omega_t}{v^2-\omega_t^2}\right) + 2\pi\left(b-1\right) + \frac{|\rho_a| - \rho_a}{2}\pi\right], \end{cases} \tag{38}$$

where $\rho_a = \pm 1$. We point out that $\left(g_{f,t}^{[1]}, \tau_{f,t}^{[1]}\right)$ and $\left(g_{a,t}^{[1]}, \tau_{a,t}^{[1]}\right)$ are both multiple-valued for a given tuning frequency $\omega_t$ due to the optional values of $\left(\rho_f, \rho_a, b\right)$. In addition, one can conclude in light of the forms of (35), (36) and (38) that

$$\frac{g_{a,t}^{[1]} e^{-j\tau_{a,t}^{[1]}\omega_t}}{\mu\left(-\omega_t^2 + 2j\zeta_g v\omega_t\right)} = g_{f,t}^{[1]} e^{-j\tau_{f,t}^{[1]}\omega_t}, \tag{39}$$

which signifies the differences in amplitude and phase between $f_e$ and $x_a$ since the required active force $u$ to achieve complete vibration suppression is independent of control laws, see the form of (16).

**Remark 2.** The branch number $b$ corresponds to the periodic delay shift of $2b\pi/\omega_t$. To facilitate discussion, we next use $b = 1$ to define the branch that yields the smallest positive values of the tuned delays $(\tau_{f,t}^{[1]}, \tau_{a,t}^{[1]})$ regardless of $\rho_f = \pm 1$ and $\rho_a = \pm 1$. ■

### 5.2. Analysis of the tuned pairs

Still considering the coupled system (23), the variations of the tuned pairs $\left(g_{f,t}^{[1]}, \tau_{f,t}^{[1]}\right)$ that are the same for the FP-DR and the F-DR, as well as $\left(g_{a,t}^{[1]}, \tau_{a,t}^{[1]}\right)$ of the A-DR with respect to the tuning frequency $\omega_t$ for $\left(\rho_f < 0, \rho_a < 0\right)$ are shown in Fig. 4.

Let us first focus on Fig. 4(b), which depicts the first two branches $b = 1, 2$ of the tuned delays. It is obvious that both $\tau_{f,t}^{[1]}$ and $\tau_{a,t}^{[1]}$ decrease as $\omega_t$ increases, a direct result of the fact that a small time gap in the high-frequency band can yield a large difference of

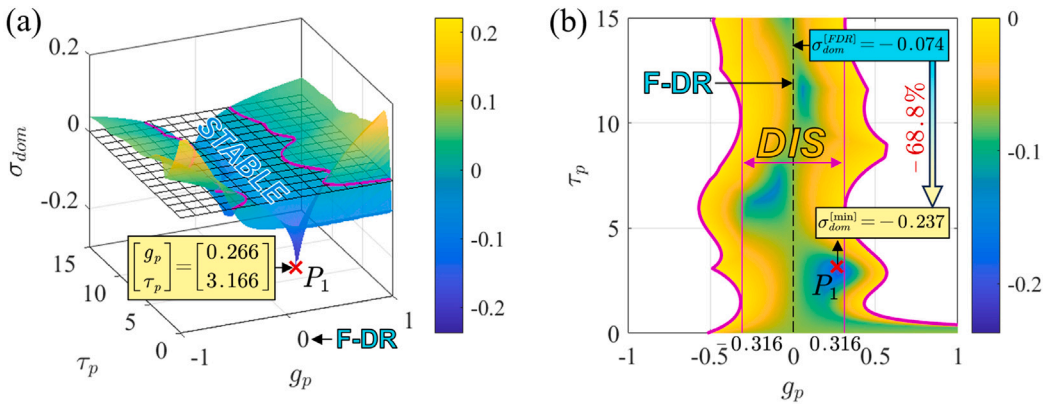


**Fig. 5.** (a). Variations of $\sigma_{dom}$ with respect to $(g_p, \tau_p)$ for the coupled system (23). Grids represent $\sigma_{dom} = 0$. (b). 2D color map focusing on the stable region ($\sigma_{dom} < 0$). DIS represents delay-independent stable. $g_p = 0$ corresponds to the F-DR.

state phase. However, this can result in an unfavorable consequence limiting the practical applications of the A-DR, i.e., the tuned delay in the high-frequency band is too small to be practically implemented [13]. In contrast, FP-DR and F-DR always exhibit a larger delay as $\tau_{f,t}^{[1]} > \tau_{a,t}^{[1]}$, which can be analytically proved by the condition (39) given $\measuredangle\left(-\omega_t^2 + 2j\zeta_g \upsilon \omega_t\right) \in [0, \pi]$. On the other hand, one can prolong the tuned delay by increasing the branch number $b$, as signified by the upward delay shifts marked in Fig. 4(b), whereas it usually leads to stability issues when adopting the A-DR [15]. As for the FP-DR, system stability can be guaranteed by selecting the pair of $(g_p, \tau_p)$, which governs the feedback force $u_p$, within the stable region in Fig. 3. Besides, the system is always stable in the F-DR case with $g_p = 0$, as aforementioned.

Then, from the tuned gain parameters $\left(g_{f,t}^{[1]}, g_{a,t}^{[1]}\right)$ shown in Fig. 4(a), the gain amplitudes in both cases are minimized around $\omega_t = \upsilon$ since it corresponds to the natural frequency of the passive absorber so a smaller active force $|u|$ is required to resonate the passive absorber to achieve complete vibration suppression. Furthermore, the amplitudes of $g_{f,t}^{[1]}$ and $g_{a,t}^{[1]}$ differ much in the low- and high-frequency bands. To explain this, we let $\left|x_p\right| = 0$ or $\left|\bar{x}_p\right| = 0$, so Eq. (1) reduces to

$$\begin{cases} \bar{m}_a \ddot{\bar{x}}_a + \bar{c}_g \dot{\bar{x}}_a + \bar{c}_a \dot{\bar{x}}_a + \bar{k}_a \bar{x}_a = \bar{u}, \\ -\left(\bar{c}_a \dot{\bar{x}}_a + \bar{k}_a \bar{x}_a\right) = \bar{f}_e - \bar{u}, \end{cases} \tag{40}$$

which corresponds to the dimensional form of (16). Note that the first equation of (40) governs the dynamics of the SDOF absorber in Fig. 1(b), and the second one indicates that all dynamic forces on the primary structure are neutralized, an obvious condition for complete vibration suppression $\left|\bar{x}_p\right| = 0$. The dimensional form of (17) leads to

$$\bar{m}_a \ddot{\bar{x}}_a + \bar{c}_g \dot{\bar{x}}_a = \bar{f}_e \Rightarrow \left|\bar{x}_a\right| = \frac{\left|\bar{f}_e\right|}{\sqrt{\left(\bar{m}_a \bar{\omega}^2\right)^2 + \left(\bar{c}_g \bar{\omega}\right)^2}}, \tag{41}$$

which indicates that the absorber motion amplitude $\left|x_a\right|$ is large and small in the low- and high-frequency bands, respectively. Since $\left(\bar{c}_a, \bar{k}_a\right)$ and $\left|\bar{f}_e\right|$ are constant in the second equation of (40), $\left|g_{a,t}^{[1]}\right|$ governing the amplitude of $u_a$ should follow the opposite variations of $\left|x_a\right|$ in the A-DR case. On the other hand, since $u_f$ of the FP-DR and F-DR is based on $f_e$ that is independent of $x_a$, $\left|g_{f,t}^{[1]}\right|$ should follow the amplitude variations of $\left|x_a\right|$, agreeing with Fig. 4(a).

### 5.3. Spectrum-based optimization by tuning $(g_p, \tau_p)$

We next investigate the benefits of the feedback force $u_p$ from the spectral perspective following [9,10,12]. Since $(g_p, \tau_p)$ appear in the characteristic Eq. (26), they affect spectral distribution although do not affect $\left(g_{f,t}^{[1]}, \tau_{f,t}^{[1]}\right)$. The duration of 98% reduction of the transient responses is used to estimate the settling time, say $t_s$ in the dimensionless form as per (2). Then,

$$e^{\sigma_{dom} t_s} < 0.02 \Rightarrow t_s = -\frac{4}{\sigma_{dom}}, \sigma_{dom} < 0, \tag{42}$$

where $\sigma_{dom} = \mathrm{Re}\left(s_{dom}\right)$, with $s_{dom}$ denoting the dominant (i.e., the rightmost) pair of characteristic roots of Eq. (26). Clearly, a smaller $\sigma_{dom}$ is preferred. Fig. 5 shows the variations of $\sigma_{dom}$ with respect to $(g_p, \tau_p)$ for the system (23) using the QPmR (quasi-polynomial root-finder) method [58].

First, Fig. 5 also reflects system stability with respect to $(g_p, \tau_p)$. The stable cases $\sigma_{dom} < 0$ in Fig. 5(a) are extracted in Fig. 5(b). The results verify the previous stable and DIS regions in Fig. 3. Then, properly designing $(g_p, \tau_p)$ can reduce $\sigma_{dom}$, yielding a minimum $\sigma_{dom}^{[\min]} = -0.237$ at $(g_p, \tau_p) = (0.266, 3.166)$, i.e., $P_1$ in Fig. 5. Note that $g_p = 0$ corresponds to the F-DR case where no

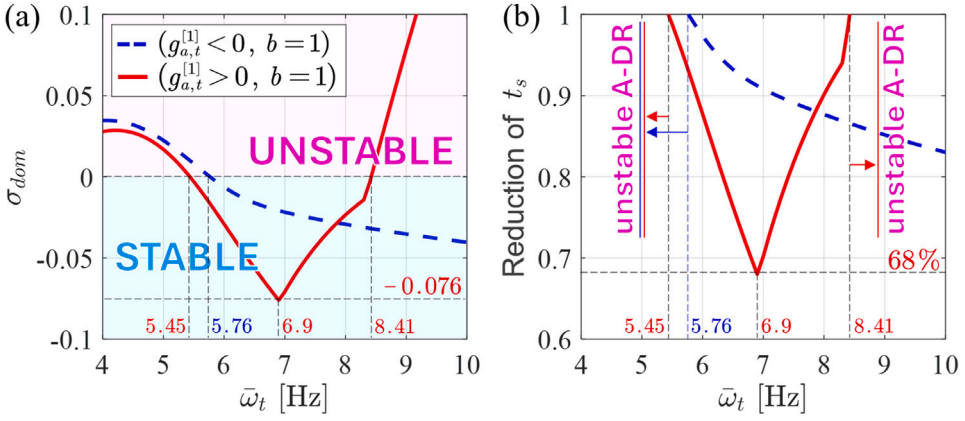


**Fig. 6.** (a). Variations of $\sigma_{dom}$ with respect to $\bar{\omega}_t = \omega\bar{\omega}_p$ in the A-DR case for the coupled system (23). (b). Reduction of the settling time $t_s$ of the A-DR by the FP-DR optimized with $(g_p, \tau_p) = (0.266, 3.166)$ to achieve $\sigma_{dom}^{[\min]}$ as per Fig. 5.

feedback force $u_p$ is deployed, and we have $\sigma_{dom}^{[FDR]} = -0.074$ in this case in light of Fig. 5(b). Comparing $\sigma_{dom}^{[FDR]}$ with $\sigma_{dom}^{[\min]}$ based on (42), one can conclude that introducing and properly designing the feedback force $u_p$ can reduce the settling time $t_s$ in the F-DR case by 68.8%, as marked in Fig. 5(b). Furthermore, the observation that the minimum $\sigma_{dom}^{[\min]}$ is achieved with $\tau_p \neq 0$ again demonstrates the benefits of taking the delay as a control parameter, and it is a counter-intuitive conclusion that increasing the state delay of the primary structure in the feedback force $u_p$ can help expedite the settlement of the primary itself. Next, the variations of $\sigma_{dom}$ in the A-DR case are shown in Fig. 6(a).

Different from Fig. 5, $\sigma_{dom}$ in Fig. 6(a) concerning the A-DR now varies with the tuning frequency $\bar{\omega}_t$ since $\left(g_a^{[1]}, \tau_a^{[1]}\right)$ must be tuned as per (38) to achieve complete vibration suppression (see Fig. 4) and since $\left(g_a^{[1]}, \tau_a^{[1]}\right)$ appear in the characteristic equation as per (14). In this example, both cases $g_{a.t}^{[1]} < 0$ and $g_{a.t}^{[1]} > 0$ with $\tau_{a.t}^{[1]}$ at $b = 1$ are considered. From the limited frequency interval where $\sigma_{dom} < 0$, the operable frequency bands of the A-DR in both cases are bounded due to stability issues. This reflects the strength of the proposed FP-DR to extend the operable frequency band of the A-DR given that system stability at any stable pair of $(g_p, \tau_p)$ in Fig. 5 holds regardless of $\bar{\omega}_t$.

On the other hand, $\sigma_{dom}$ in the A-DR case exhibits a minimum at $\sigma_{dom} = \sigma_{dom}^{[ADR]} = -0.076$ when $\bar{\omega}_t = 6.9$ Hz. Given $\sigma_{dom}^{[ADR]} \approx \sigma_{dom}^{[FDR]}$, the proposed FP-DR, even if it is purely feedforward-controlled with $u_p = 0$, can expedite the response speed of the A-DR in the entire frequency band. Focusing on the operable frequency band of the A-DR, Fig. 6(b) further shows that the FP-DR achieving $\sigma_{dom}^{[\min]}$ beneficially reduces the settling time $t_s$ of the A-DR by up to 68% at least.

### 5.4. Frequency response optimization by tuning $(g_p, \tau_p)$

The distribution of dominant roots $s_{dom}$ signified by $\sigma_{dom}$ reflects system performance in the transient process. To exploit the benefits of the FP-DR in steady states, we consider the frequency response curves governed by the amplitude

$$A_G(\omega) = \left| G_{fe\to xp}(s = j\omega) \right|, \tag{43}$$

where $G_{fe\to xp}$ is defined in (11). Focusing on $\bar{\omega}_t = 6.9$ Hz, where the A-DR tuned with $(\rho_a > 0, b = 1)$, or more specifically, $\left(g_{a,t}^{[1]}, \tau_{a,t}^{[1]}\right) = (0.233, 3.655)$, yields a minimum of $\sigma_{dom}$ as per Fig. 6(a), the variations of $A_G$ in several elaborated cases with a passive absorber, a tuned A-DR, a tuned F-DR, and a tuned FP-DR for the coupled system (23) are shown in Fig. 7(a).

From the frequency response curve $C_1$ in Fig. 7(a), a passive vibration absorber creates an antiresonance valley around its natural frequency $\bar{\omega}_a = 6.11$ Hz, whereas the resulting vibration suppression is far from complete. Once a tuned A-DR is activated, the resulting curve $C_2$ exhibits an antiresonance valley and an ideal zero antiresonance point at the designated tuning frequency $\bar{\omega}_t$ independent of $\bar{\omega}_a$. Besides, the F-DR ($g_p = 0$) and the FP-DR ($g_p \neq 0$) tuned with $(\rho_f > 0, b = 1)$, i.e., $\left(g_{f,t}^{[1]}, \tau_{f,t}^{[1]}\right) = (0.355, 0.751)$, are also considered, which achieve the zero antiresonance at $\bar{\omega}_t$ for complete vibration suppression independent of the $(g_p, \tau_p)$ values that govern the feedback force $u_p$, agreeing with (37).

Clearly, a broader antiresonance valley helps suppress residual vibrations in practice by lowering the response sensitivity of the primary. On the other hand, the resonance peaks should also be limited to control the maximum vibrations to reduce the risks of possible resonance perturbations [59,60]. Following [46], we define the height of the resonance peaks as

$$h = \max\left\{A_G(\omega)\right\}, \tag{44}$$

and define the width of the antiresonance valley as

$$W\left(A_G^{[V]}\right) = \omega_2 - \omega_1, \tag{45}$$

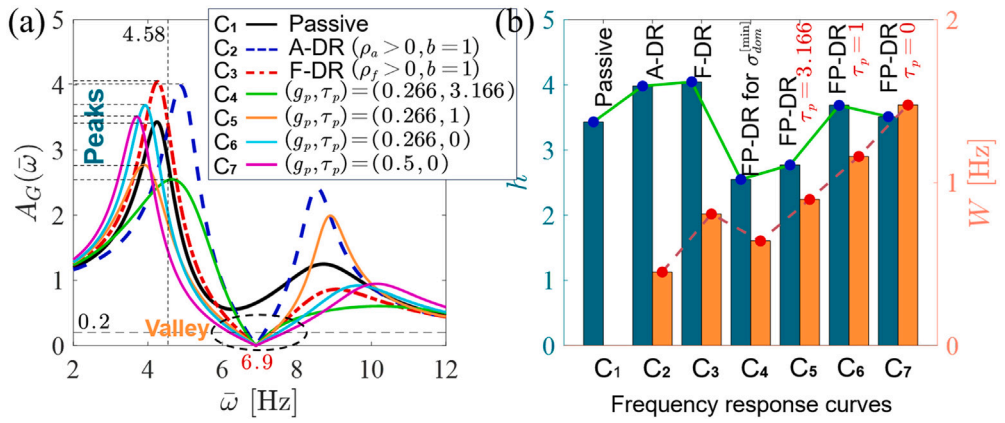


**Fig. 7.** (a). Frequency responses of the primary structure concerning the coupled system (23) for various parametric compositions. The A-DR, F-DR, and FP-DR adopted in cases $C_2$-$C_6$ are tuned with $(\rho_a, \rho_f > 0, b = 1)$. (b). Comparisons of the height of resonance peaks and the width of the antiresonance valley for different frequency response curves in (a).

where $A_G^{[V]}$ needs to be specified, and $(\omega_1, \omega_2)$ are the two frequencies closest to $\omega_t$ additionally satisfying

$$\begin{cases} \omega_1 < \omega_t < \omega_2, \\ A_G(\omega_1) = A_G(\omega_2) = A_G^{[V]}. \end{cases} \tag{46}$$

Note that a smaller $h$ and a larger $W$ are preferred. We select $A_G^{[V]} = 0.2$ for the cases in Fig. 7(a), and the associated values of $(h, W)$ are summarized in Fig. 7(b). Comparing curves $C_2$ and $C_3$, the F-DR increases $W$ while slightly raising $h$ compared to the A-DR. Furthermore, the FP-DR achieving $\sigma_{dom}^{[min]}$ as per Fig. 5 for the shortest settling time $t_s$ corresponds to $C_4$, which increases $W$ while reducing $h$, thus enhancing the performance of the A-DR in both transient processes and steady states. Curves $(C_5, C_6, C_7)$ evaluate the effects of the feedback force $u_p$ governed by $(g_p, \tau_p)$ on the FP-DR, and one can conclude that increasing $g_p$ while reducing $\tau_p$ helps extend the antiresonance valley to suppress residual vibrations. However, revisiting Figs. 3 and 5, the increase in $g_p$ outside the DIS region (33) should be limited to avoid a narrow stable interval of $\tau_p$ and thus to benefit the control robustness against destabilization due to delay perturbations.

Next, we investigate the behaviors of $(h, W)$ in more general cases by sweeping $\bar{\omega}_t$ within the operable frequency band of the A-DR according to Fig. 6. Fig. 8(a, b) show the case $(\rho_a, \rho_f > 0, b = 1)$, where the marked frequency $\bar{\omega}_t = 6.9$ Hz corresponds to the results in Fig. 7. Besides, the case $(\rho_a, \rho_f < 0, b = 1)$ is depicted in Fig. 8(c, d). From Fig. 8(a, c), the F-DR and FP-DR do not significantly raise the resonance peak $h$ of the A-DR, and instead, $h$ can be significantly reduced at most frequencies. Then, from Fig. 8(b, d) for the width $W$ of the antiresonance valley, the F-DR and the optimized FP-DR for $\sigma_{dom}^{[min]}$ can possibly reduce $W$, although they can both expedite the response speed of the A-DR as per in Figs. 5 and 6. Alternatively, the FP-DR with $(g_p, \tau_p) = (0.5, 0)$ yields a large $W$ within a sufficiently broad frequency band. To maximize the performance of the FP-DR, one can switch the two control parameters $(g_p, \tau_p)$ to achieve $\sigma_{dom}^{[min]}$ in the transient process for reducing $t_s$ and to extend $W$ while limiting $h$ in the steady states for suppressing residual vibrations.

At last, comparisons between Figs. 6 and 8 suggest that tuning A-DR needs to handle the trade-off of gain polarity between the positive case $\rho_a > 0$ for smaller values of $(h, \sigma_{dom})$ and the negative case $\rho_a < 0$ for a broader operable frequency band plus a larger $W$. Hence, it can increase the implementation complexity as the excitation frequency varies. As for the FP-DR, the operable frequency band and $\sigma_{dom}$ both only depend on the feedback force $u_p$, and thus $\rho_f$ governing the polarity of the feedforward force $u_f$ only needs to be determined as per $(h, W)$, thus simplifying the analysis. Comparing Figs. 8(a, b) and 8(c, d), one can simply apply $\rho_f > 0$ within the whole frequency band when adopting the FP-DR for the given system (23).

## 6. Complete suppression of multiple-frequency vibrations

To completely suppress the multiple-frequency vibration with $P$ $(P \in \mathbb{Z}^+, P \geqslant 2)$ frequency components, Eq. (13) must have $P$ solutions of $\omega_t$ lying at such components. Note that the degree of Eq. (13) is two when no delayed control terms are used, and thus a single single-mass absorber driven by a non-delayed control law can only handle single-frequency vibrations ($P = 1$). Alternatively, the equation degree (i.e., system order) raised by exponents makes it possible to handle the case $P \geqslant 2$ while keeping linearity, reflecting the unique strength of delayed control. Existing work [48] based on the A-DR will be compared.

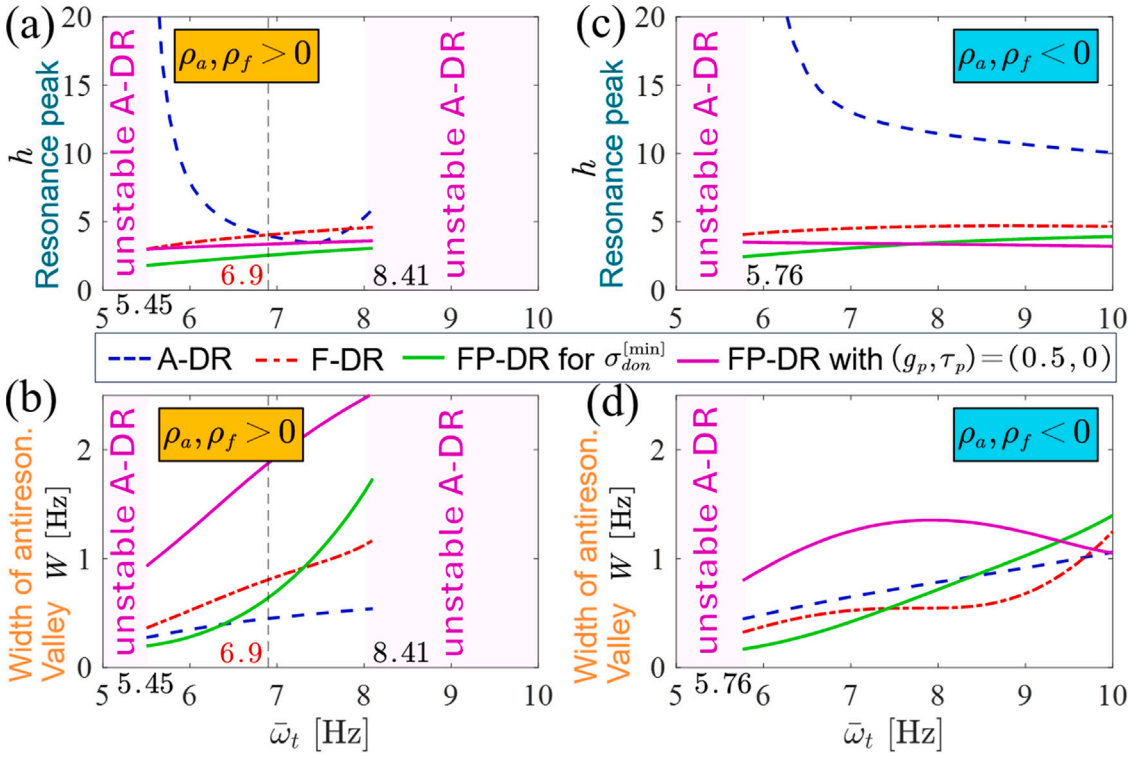


**Fig. 8.** Variations of $(h, W)$ associated with several tuned A-DR, F-DR, and FP-DR versus the tuning frequency $\bar{\omega}_t$ within the operable frequency band of the A-DR as per Fig. 6. (a, b). The case $(\rho_a, \rho_f > 0, b = 1)$. (c, d). The case $(\rho_a, \rho_f < 0, b = 1)$. FP-DR for $\sigma_{dom}^{[\min]}$ corresponds to $(g_p, \tau_p) = (0.266, 3.166)$. The example is based on the system (23).

### 6.1. Tuning mechanism of the FP-DR

When adopting the FP-DR, substituting $U_f$ in (25) into (13) yields

$$\begin{aligned} N\left(j\omega_t, g_f^{[1,\ldots,N_f]}, g_f^{[1,\ldots,N_f]}\right) =& j\mu\upsilon\left(2\zeta_a\omega_t + \upsilon\right)\sum_{i=1}^{N_f} g_f^{[i]} e^{-j\tau_f^{[i]}\omega_t} \\ &+ \left(1 - \sum_{i=1}^{N_f} g_f^{[i]} e^{-j\tau_f^{[i]}\omega_t}\right)\left[\mu\left(-\omega_t^2 + 2j\left(\zeta_a + \zeta_g\right)\upsilon\omega_t + \upsilon^2\right)\right] = 0, \end{aligned} \tag{47}$$

which is expected to have $P$ solutions of $\omega_t \in \mathbb{R}^+$ at the given $P$ frequency components. We rewrite Eq. (47) as

$$\sum_{i=1}^{N_f} g_f^{[i]} e^{-j\tau_f^{[i]}\omega_t^{[p]}} = \sigma_p\left(\omega_t^{[p]}\right) + j\varpi_p\left(\omega_t^{[p]}\right), \tag{48}$$

where $\omega_t^{[p]}$, $p = 1, 2, \ldots, P$, corresponds to the frequency components, and $\left(\sigma_p, \varpi_p\right) \in \mathbb{R}^2$ result from

$$\sigma_p\left(\omega_t^{[p]}\right) + j\varpi_p\left(\omega_t^{[p]}\right) = \frac{\upsilon^2 - \left(\omega_t^{[p]}\right)^2 + 2j\left(\zeta_a + \zeta_g\right)\upsilon\omega_t^{[p]}}{-\left(\omega_t^{[p]}\right)^2 + 2j\zeta_g\upsilon\left(\omega_t^{[p]}\right)^2}. \tag{49}$$

Note that Eq. (48) is the general form of (35). Clearly, one solution of $\omega_t$ corresponds to two real equations stemming from the real and imaginary parts of Eq. (48), and thus handling $P$ frequency components $\omega_t^{[1,\ldots,P]}$ necessitates $N_f \geqslant P$. Here, we let $N_f = P$ to minimize the number of control terms to enhance control robustness, yielding $2P$ control parameters $\left(g_f^{[1,\ldots,P]}, \tau_f^{[1,\ldots,P]}\right)$ to be tuned

as per $\omega_t^{[1,\dots,P]}$. In this case, Eq. (48) can be expanded into $2P$ real equations as

$$\begin{cases} \sum_{i=1}^{P} g_{f,t}^{[i]} \cos\left(\tau_{f,t}^{[i]}\omega_t^{[p]}\right) = \sigma_p\left(\omega_t^{[p]}\right), \\ \sum_{i=1}^{P} g_{f,t}^{[i]} \sin\left(\tau_{f,t}^{[i]}\omega_t^{[p]}\right) = -\varpi_p\left(\omega_t^{[p]}\right), \end{cases} \quad p = 1, 2, \dots, P. \tag{50}$$

Hence, the tuned control parameters $\left(g_{f,t}^{[1,\dots,P]}, \tau_{f,t}^{[1,\dots,P]}\right)$ can be numerically determined. However, the periodicity of trigonometric functions in Eq. (50) leads to multiple solutions, which can be unfavorable to the solving process. To this end, we confine the search region of $\tau_{f,t}^{[i]}$ using the concept of the branch number $b \in \mathbb{Z}^+$ in (37) and (38) by defining the $b$th branch as

$$\frac{2(b-1)\pi}{\omega_t^{[\max]}} < \tau_{f,t}^{[i]} < \frac{2b\pi}{\omega_t^{[\max]}}, \tag{51}$$

where $\omega_t^{[\max]} = \max\left\{\omega_t^{[1]}, \omega_t^{[2]}, \dots, \omega_t^{[P]}\right\}$. Besides, we stress that different from the single-frequency case $P = 1$ in Section 5.1, the shifted tuned delays $\tau_{f,t}^{[i]} \pm 2\pi/\omega_t^{[p]}$ are no longer solutions of (50) due to the coupling between $\tau_{f,t}^{[1,\dots,P]}$ and $\omega_t^{[1,\dots,P]}$. This means that when $P \geqslant 2$, one cannot simply shift $\tau_{f,t}^{[i]}$ to satisfy the possible hardware requirement $\tau_{f,t}^{[i]} > \tau_{loop}$, where $\tau_{loop} > 0$ is the inherent loop delay.

### 6.2. Tuning mechanism of the A-DR

For the A-DR driven by the feedback control logic (4) in terms of $\left(g_a^{[i]}, \tau_a^{[i]}\right)$, one following (48) and (49) can arrive at

$$\sum_{i=1}^{N_a} g_a^{[i]} e^{-j\tau_a^{[i]}\omega_t^{[p]}} = \mu\left(v^2 - \left(\omega_t^{[p]}\right)^2 + 2j\left(\zeta_a + \zeta_g\right)v\omega_t^{[p]}\right), \tag{52}$$

which agrees with (39) given (49). We first consider the case $N_a = P$ to minimize the number of control terms as the FP-DR in (50), yielding $2P$ control parameters $\left(g_a^{[1,\dots,P]}, \tau_a^{[1,\dots,P]}\right)$ to be tuned as per

$$\begin{cases} \sum_{i=1}^{P} g_{a,t}^{[i]} \cos\left(\tau_{a,t}^{[i]}\omega_t^{[p]}\right) = \mu\left(v^2 - \left(\omega_t^{[p]}\right)^2\right), \\ \sum_{i=1}^{P} g_{a,t}^{[i]} \sin\left(\tau_{a,t}^{[i]}\omega_t^{[p]}\right) = -2\mu\left(\zeta_a + \zeta_g\right)v\omega_t^{[p]}, \end{cases} \quad p = 1, 2, \dots, P, \tag{53}$$

where the tuned delays $\tau_{a,t}^{[1,\dots,P]}$ satisfying $2(b-1)\pi < \tau_{a,t}^{[i]}\omega_t^{[\max]} < 2b\pi$ are defined as the $b$th branch in light of (51).

On the other hand, Valasek et al. [48] taking a further step from [47] proposed a control logic with $N_a = 2P$ for the A-DR,

$$u_a(t) = \sum_{i=0}^{2P} g_a^{[i]} x_a\left(t - \tau_a^{[i]}\right), \tag{54}$$

where $\tau_a^{[i]} = i\tau_a^{[0]}$, in which $\tau_a^{[0]} \in \mathbb{R}^+$ needs to be artificially specified. In this case, the control parameters are the $2P$ gains $g_a^{[1,\dots,2P]}$. Similar to (53), the tuned gains can be determined as per the $2P$ equations

$$\begin{cases} \sum_{i=1}^{2P} g_{a,t}^{[i]} \cos\left(i\tau_{a,t}^{[0]}\omega_t^{[p]}\right) = \mu\left(v^2 - \left(\omega_t^{[p]}\right)^2\right), \\ \sum_{i=1}^{2P} g_{a,t}^{[i]} \sin\left(i\tau_{a,t}^{[0]}\omega_t^{[p]}\right) = -2\mu\left(\zeta_a + \zeta_g\right)v\omega_t^{[p]}, \end{cases} \quad p = 1, 2, \dots, P. \tag{55}$$

Different from (53), Eq. (55) is purely polynomial in $g_{a,t}^{[1,\dots,2P]}$ since $\left(\cos\left(i\tau_{a,t}^{[0]}\omega_t^{[p]}\right), \sin\left(i\tau_{a,t}^{[0]}\omega_t^{[p]}\right)\right)$ are real values once $\left(\tau_a^{[0]}, \omega_t^{[p]}\right)$ are given, thus simplifying the solving process. For discrimination, we call the A-DR corresponding to (53) and (55) as A-DR-1 and A-DR-2, respectively. Note that the simplified tuning mechanism of A-DR-2 compromises the increased number of control terms (i.e., $P$ terms for A-DR-1 and $2P$ terms for A-DR-2), although such two A-DRs have the same number ($2P$) of control parameters, and thus trade-offs need to be considered in practical applications.

### 6.3. Stability analysis in the A-DR case

As per Section 3.2, system stability in the FP-DR case can be guaranteed by selecting $(g_p, \tau_p)$ within the stable region in Figs. 3 or 5, independent of the values of $\left(g_f^{[1,\dots,P]}, \tau_f^{[1,\dots,P]}\right)$. Besides, the FP-DR with $g_p = 0$ reduces to the F-DR, which is always stable. In this part, we investigate the stability issues when adopting the A-DR to handle multiple-frequency vibrations $P \geqslant 2$. Still focusing on the system (23), we consider the case $P = 2$ for demonstration. For the A-DR-1, the tuned pairs $\left(g_{a,t}^{[1]}, g_{a,t}^{[2]}, \tau_{a,t}^{[1]}, \tau_{a,t}^{[2]}\right)$ following (53) are shown in Fig. 9, where $\left(\tau_{a,t}^{[1]}, \tau_{a,t}^{[2]}\right)$ at the smallest branch $b$ are sought.

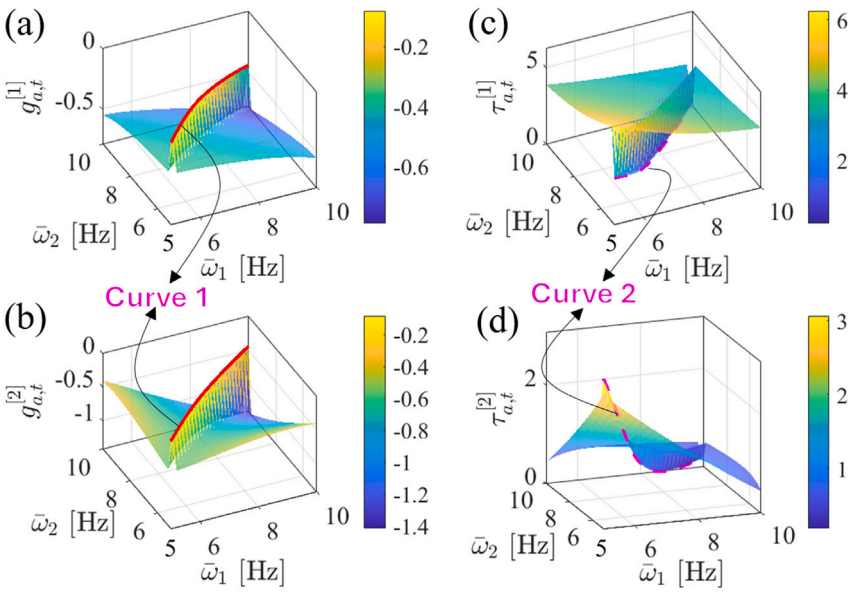


**Fig. 9.** Variations of the tuned pairs $\left(g_{a,t}^{[1]}, g_{a,t}^{[2]}, \tau_{a,t}^{[1]}, \tau_{a,t}^{[2]}\right)$ of the A-DR-1 when $P = 2$ with respect to $\left(\bar{\omega}_t^{[1]}, \bar{\omega}_t^{[2]}\right)$ for the system (23). (a). Variations of $g_{a,t}^{[1]}$. (b). Variations of $g_{a,t}^{[2]}$. (a). Variations of $\tau_{a,t}^{[1]}$. (d). Variations of $\tau_{a,t}^{[2]}$. Curves 1 and 2 correspond to the reduced case $\bar{\omega}_t^{[1]} = \bar{\omega}_t^{[2]}$ where we let $\left(g_{a,t}^{[1]}, \tau_{a,t}^{[1]}\right) = \left(g_{a,t}^{[2]}, \tau_{a,t}^{[2]}\right)$ and $g_{a,t}^{[1]}, g_{a,t}^{[2]} < 0$ to seek numerical solutions.

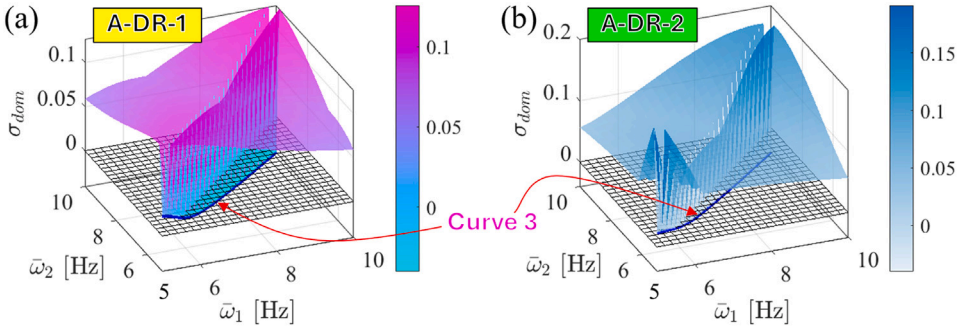


**Fig. 10.** Variations of $\sigma_{dom}$ with respect to $\left(\bar{\omega}_t^{[1]}, \bar{\omega}_t^{[1]}\right)$ for the coupled system (23). (a). A-DR-1 case corresponding to (53). Tuned pairs $\left(g_{a,t}^{[1]}, g_{a,t}^{[2]}, \tau_{a,t}^{[1]}, \tau_{a,t}^{[2]}\right)$ follow Fig. 9. (b). A-DR-2 case corresponding to (55) with $\tau_a^{[0]} = 1$. Grids denote $\sigma_{dom} = 0$.

From Fig. 9, $\left(g_{a,t}^{[1]}, g_{a,t}^{[2]}, \tau_{a,t}^{[1]}, \tau_{a,t}^{[2]}\right)$ are all symmetrical about the line $\bar{\omega}_t^{[1]} = \bar{\omega}_t^{[2]}$ since a linear dual-frequency excitation is the superposition of two single-frequency excitations at $\bar{\omega}_t^{[1]}$ and $\bar{\omega}_t^{[2]}$. Particularly, to avoid solution multiplicity of (53) when $\bar{\omega}_t^{[1]} = \bar{\omega}_t^{[2]}$, we let $\left(g_{a,t}^{[1]}, \tau_{a,t}^{[1]}\right) = \left(g_{a,t}^{[2]}, \tau_{a,t}^{[2]}\right)$ with $g_{a,t}^{[1]}, g_{a,t}^{[2]} < 0$. Results in this reduced case are marked as Curves 1 and 2, which agree with the tuned pairs in the single-frequency case, see Eq. (37). For system stability, we substitute $\left(g_{a,t}^{[1]}, g_{a,t}^{[2]}, \tau_{a,t}^{[1]}, \tau_{a,t}^{[2]}\right)$ into (14) and calculate the real part $\sigma_{dom}$ of the dominant roots $s_{dom}$ following Fig. 5, yielding Fig. 10(a).

Curve 3 in Fig. 10(a) corresponds to the case $\bar{\omega}_t^{[1]} = \bar{\omega}_t^{[2]}$, and it concurs with the blue dashed curve in Fig. 6(a), as expected. One can find that no stable region appears when $\bar{\omega}_t^{[1]} \neq \bar{\omega}_t^{[2]}$, indicating that the A-DR-1 is inoperable to handle multiple-frequency vibrations. As for the A-DR-2, we select $\tau_a^{[0]} = 1$ in (55) for instance. Following the same analysis procedure as the A-DR-1, variations of $\sigma_{dom}$ with respect to $\left(\bar{\omega}_t^{[1]}, \bar{\omega}_t^{[2]}\right)$ in the A-DR-2 case are shown in Fig. 10(b), where Curve 3 for $\bar{\omega}_t^{[1]} = \bar{\omega}_t^{[2]}$ concurs with the namesake one in Fig. 10(a). However, stable regions still do not exist when $\bar{\omega}_t^{[1]} \neq \bar{\omega}_t^{[2]}$. Since the A-DR-2 has a manipulatable parameter $\tau_a^{[0]}$, we now sweep $\tau_a^{[0]}$ while fixing $\left(\bar{\omega}_t^{[1]}, \bar{\omega}_t^{[2]}\right) = (6.5\text{ Hz}, 8.5\text{ Hz})$ to search stable regions. The resulting variations of $\sigma_{dom}$ with respect to $\tau_a^{[0]}$ are shown in Fig. 11.

From Fig. 11, a stable system requiring $\sigma_{dom} < 0$ is still unavailable, although both frequencies (6.5 Hz, 8.5 Hz) are operable in the single-frequency case as per Fig. 6(a). Further attempts to seek operable control parameters include re-designing the structural

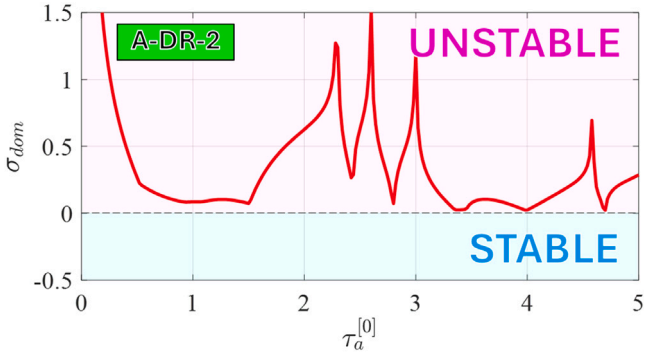


**Fig. 11.** Variations of $\sigma_{dom}$ with respect to $\tau_a^{[0]}$ for the A-DR-2 of the coupled system (23) to handle dual-frequency vibration with $\left(\bar{\omega}_t^{[1]}, \bar{\omega}_t^{[2]}\right) = (6.5\text{ Hz}, 8.5\text{ Hz})$. A stable system requires $\sigma_{dom} < 0$.

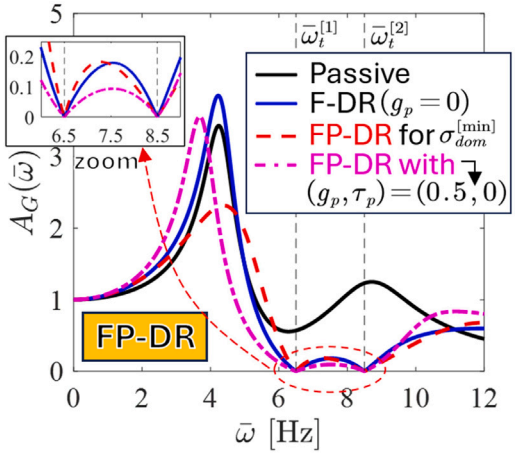


**Fig. 12.** Frequency responses of the primary structure for the coupled system (23) with an F-DR or FP-DR tuned as per $\left(\bar{\omega}_t^{[1]}, \bar{\omega}_t^{[2]}\right) = (6.5\text{ Hz}, 8.5\text{ Hz})$ and $b = 1$. $\sigma_{dom}^{[\min]}$ corresponds to $(g_p, \tau_p) = (0.266, 3.166)$.

parameters or the control laws (e.g., the fixed delay parameters in (54)), which, however, are still open problems, as also pointed out in [48]. Consequently, the applicability of the classical A-DR techniques can be limited.

On the other hand, based on the analysis procedures here, one can further conclude that even if an absorber-based feedback control logic exists to yield operable control parameters in the multiple-frequency case $P \geqslant 2$, the application of the corresponding A-DR can still be challenging given the complexity in analyzing system stability, or more specifically, in determining such operable control parameters. The reason is that no analytical methods exist to intuitively determine operable control parameters as Fig. 3 and the numerical sweeping procedures as Fig. 11 to examine characteristic spectrum can become inefficient as the number of delayed control terms increases. Such issues are unfavorable to real-time updating control parameters in cases where excitation frequencies can vary [61]. In comparison, the stability and spectrum analyses in the FP-DR case are rather simple, see Section 4 and Section 5.3.

### 6.4. Frequency response analysis in the FP-DR case

As aforementioned, stability and spectrum analyses in the FP-DR case completely solved in Figs. 3 and 5 hold regardless of the values of $\left(g_f^{[i]}, \tau_f^{[i]}\right)$ and thus the number of frequency components. We now investigate the frequency responses of the primary structure in the FP-DR case and show how can the feedback force $u_p$ governed by $(g_p, \tau_p)$ enhance the performance. Still focusing on the example $\left(\bar{\omega}_t^{[1]}, \bar{\omega}_t^{[2]}\right) = (6.5\text{ Hz}, 8.5\text{ Hz})$, we have $\left(g_{f,t}^{[1]}, g_{f,t}^{[2]}, \tau_{f,t}^{[1]}, \tau_{f,t}^{[2]}\right) = (0.805, 0.508, 0.761, 3.569)$ when $b = 1$ as per (50) for tuning both the FP-DR and its reduced case F-DR, see also Fig. 9. The resulting frequency response curves for several stable pairs of $(g_p, \tau_p)$ following (43) and Fig. 7 are shown in Fig. 12.

From Fig. 12, the desired zero antiresonance at the given frequencies $\left(\bar{\omega}_t^{[1]}, \bar{\omega}_t^{[2]}\right) = (6.5\text{ Hz}, 8.5\text{ Hz})$ is achieved in both the F-DR and the FP-DR cases, as expected. Note that achieving multiple ideal zero antiresonance points by the F-DR and the FP-DR does not compromise the raised resonance peaks compared with the passive case. Particularly, two pairs of $(g_p, \tau_p)$ are considered for

the FP-DR following Fig. 8. One is $(g_p, \tau_p) = (0.266, 3.166)$, which achieves $\sigma_{dom}^{[\min]}$ for the minimum settling time $t_s$ as per Fig. 5 and (42). We reiterate that $\sigma_{dom}^{[\min]}$ holds regardless of the single- and multiple-frequency cases. One can find that reducing $t_s$ of the F-DR by the FP-DR can possibly narrow the antiresonance valley at the tuning frequency $\bar{\omega}_t^{[i]}$. The solution is simple to switch $(g_p, \tau_p)$ in steady states similar to the single-frequency case in Section 5.4. The given example $(g_p, \tau_p) = (0.5, 0)$ shows that increasing $g_p$ while reducing $\tau_p$ can also extend multiple antiresonance valleys at multiple frequencies thus enhancing the vibration suppression in steady states, as to be experimentally verified next.

**Remark 3.** Increasing $g_p$ and reducing $\tau_p$ to suppress residual vibrations can also be explained from the perspective of reducing the effects of nonlinear frictions. In our model (1), the energy dissipation due to the contacts between the mechanical components and slides is incorporated into linear damping. However, when the velocity switches direction, i.e., $(\dot{x}_p, \dot{x}_a) \to (0, 0)$, the nonlinear effects become dominant [20]. For the absorber, such effects can be omitted since $\dot{x}_a = 0$ corresponds to the maximum displacement $x_a = |x_a|$, with $|x_a|$ denoting amplitude, so the absorber is subjected to the maximum restoring force for returning to $x_a = 0$. Since complete vibration suppression is to neutralize the dynamical forces on the primary structure, the nonlinear frictions can have more significant effects on $x_p$ in the states of near-complete vibration suppression $|x_p| \approx 0_+$ thus resulting in (nonlinear) residual vibrations. Beneficially, the feedback force $u_p$ with $g_p > 0$ and $\tau_p \to 0$ pushes the primary structure back to $x_p = 0$ once $x_p \neq 0$ so the absolute value of $\dot{x}_p$ is increased at $x_p = 0$, thus reducing the effects of the nonlinear frictions. We point out that when the frequency is sufficiently low as $\omega \to 0$, the nonlinear frictions at $x_p = 0$ can significantly affect complete vibration suppression since $|\dot{x}_p|$ of the residual vibrations is now small, making nonlinear frictions dominant around $x_p = 0$. However, the ultra-low-frequency vibration suppression combined with nonlinear frictions deserves a new study topic, which is beyond the scope of the present paper. One can refer to [20] for further information. ■

## 7. Verifications

We have theoretically shown that the FP-DR outperforms the F-DR and A-DR for complete suppression of both the single- and multiple-frequency vibrations. Numerical simulation and experimental tests are conducted here for verifications. Particularly, the SIMULINK-based simulation models used and video recordings of the experiments are available in Appendix A.

### 7.1. Experimental condition

The mechanical body of the experimental setup following Fig. 1 is shown in Fig. 13(a, b). Two laser sensors are fixed on the frame to monitor the absolute displacements $(\bar{x}_p, \bar{x}_a)$ of the primary structure and the absorber. Two voice coil motors (VCMs) are used as actuators to generate the excitation force $\bar{f}_e$ and the active force $\bar{u}$. The control loop of the VCM is shown in Fig. 13(c), where dSPACE MicroLabBox as the controller processes the laser sensor information for $(\bar{x}_p, \bar{x}_a)$ and generates control signals to VCM drivers. The drivers then amplify the control signals by inputting current to the associated VCM movers. The electromagnetic effects between the VCM mover and stator finally yield the desired forces, see also Remark 1. Note that no force sensors are used due to the limited installation space. When designing the feedforward force $\bar{u}_f$ of the FP-DR and F-DR, we indirectly measure $\bar{f}_e$ via the current of VCM1. Additional independent experiments to test the relationship between the current input and the force output of the VCM can be found in Appendix B.

Based on measurement and system identification, the structural parameters are obtained as

$$\begin{aligned} &\bar{m}_a = 0.51 \text{ kg}, \bar{c}_a = 4.3 \text{ Ns/m}, \bar{c}_g = 2.0 \text{ Ns/m}, \bar{k}_a = 753 \text{ N/m}, \\ &\bar{m}_p = 0.965 \text{ kg}, \bar{c}_p = 5.0 \text{ Ns/m}, \bar{k}_p = 1465 \text{ N/m}, \end{aligned} \tag{56}$$

which correspond to the dimensionless variables in (23). In the tests, single-frequency ($P = 1$) and dual-frequency ($P = 2$) vibrations are separately considered, and accordingly, the excitation $\bar{f}_e$ follows the form

$$\begin{cases} P = 1 : \bar{f}_e(\bar{t}) = 4 \sin(\bar{\omega}\bar{t}) \text{ N}, \\ P = 2 : \bar{f}_e(\bar{t}) = 3\left[\sin(\bar{\omega}_1\bar{t} + \phi_1) + \sin(\bar{\omega}_2\bar{t} + \phi_2)\right] \text{ N}. \end{cases} \tag{57}$$

Note that the values of $\phi_1$ and $\phi_2$ do not affect the complete vibration suppression $|\bar{x}_p| = 0$ since different $\omega_t$ solutions of Eq. (13) are independent of each other. Hence, we let $\phi_1 = \phi_2 = 0$. Besides, frequency mismatch is not considered so $\bar{\omega}_t = \bar{\omega}$. We point out that in the following tests, except for $(\bar{g}_p, \bar{\tau}_p)$, all the other control parameters, including $(\bar{g}_f^{[i]}, \bar{\tau}_f^{[i]})$ and $(\bar{g}_a^{[i]}, \bar{\tau}_a^{[i]})$, which need to be tuned to achieve complete vibration suppression, are automatically calculated as per the vibration frequency, see Eqs. (37), (38), (50), (53), and (55).

### 7.2. Single-frequency case $P = 1$: Extended operable frequency band

Let us start with the complete suppression of single-frequency vibrations. From Fig. 6(a), the operable frequency band of the A-DR is bounded regardless of the gain polarity $\rho_a$. We here test the inoperability of the A-DR in the low-frequency band by considering the unstable case $\bar{\omega} = 5.3$ Hz when $\rho_a > 0$ and $b = 1$. The A-DR following (38) is then tuned by $(g_{a.t}^{[1]}, \tau_{a.t}^{[1]}) = (0.192, 6.367)$ or equivalently, the practical values $(\bar{g}_{a.t}^{[1]}, \bar{\tau}_{a.t}^{[1]}) = (g_{a.t}^{[1]}\bar{k}_p, \tau_{a.t}^{[1]}/\bar{\omega}_p) = (281.33 \text{ N/m}, 163.4 \text{ ms})$. The resulting simulation responses of the primary structure are shown as the blue curves in Fig. 14(a, b).

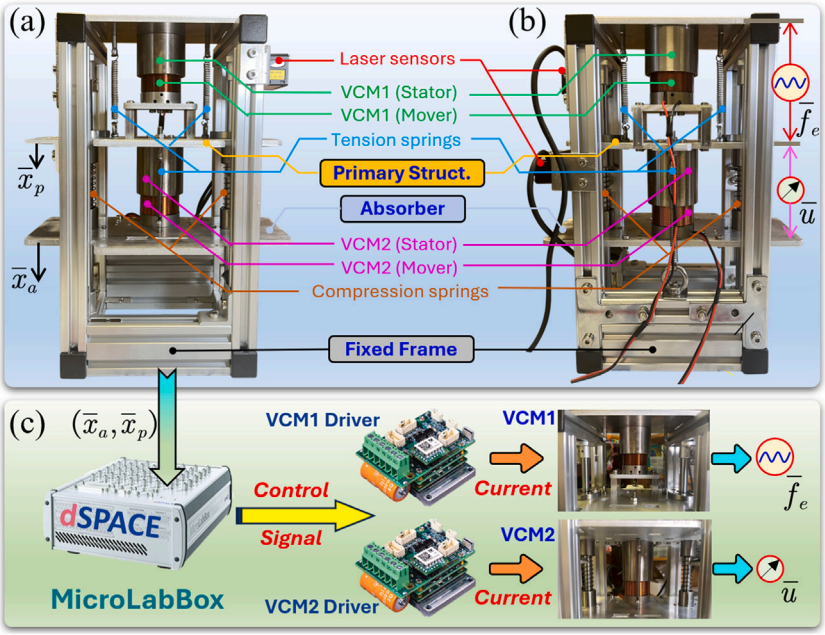


**Fig. 13.** Experimental setup. (a). Front view. (b). Back view. (c). The control loop of the VCMs (voice coil motors) for $(\bar{f}_e, \bar{u})$.

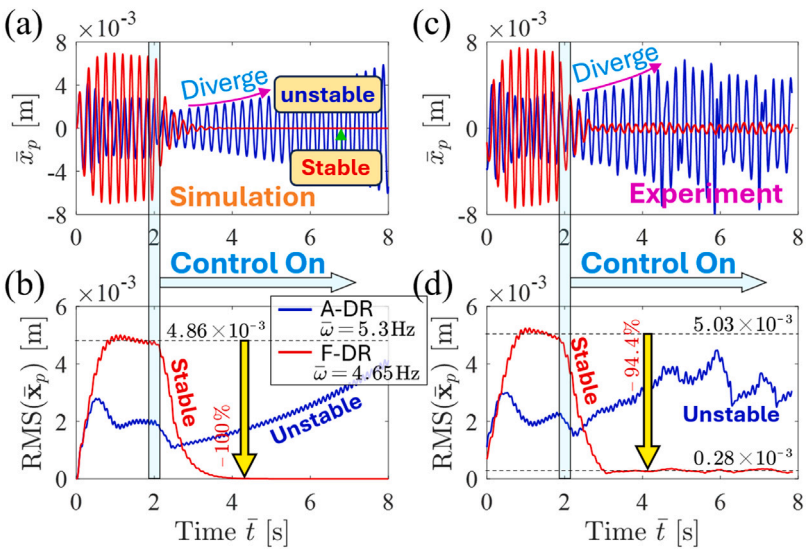


**Fig. 14.** Tests of the A-DR and F-DR for suppressing low-frequency vibration. Tuned pairs are with $\rho_a, \rho_f > 0$ and $b = 1$. Active force $u$ is activated when $\bar{t} \geqslant 2$ s. (a, b). Simulations. (c, d). Experiments. RMS in (b, d) refers to root mean squares for the dataset $\bar{\mathbf{x}}_p$ sampled within the last 0.4 s before the current time step $\bar{t}$.

From Fig. 14(a, b), the divergent responses in the A-DR case after introducing the active force at $\bar{t} = 2$s verify the instability, and thus the applications of the A-DR can be limited. Alternatively, the F-DR, which is purely feedforward-controlled, does not affect system stability. To test the low-frequency performance of the F-DR, we further reduce the excitation frequency to $\bar{\omega} = 4.65$ Hz, which is the lowest value to limit system responses within the operable working space of the experimental setup, leading to $\left(\bar{g}_{f,t}^{[1]}, \bar{\tau}_{f,t}^{[1]}\right) = \left(g_{f,t}^{[1]}, \tau_{f,t}^{[1]}/\bar{\omega}_p\right) = (0.836, 85.0 \text{ ms})$ when $\rho_f > 0$ and $b = 1$. The resulting responses of the primary structure are superposed as the red curves. This time, complete vibration suppression $\left|\bar{x}_p\right| = 0$ is achieved in steady states.

The corresponding experimental results are shown in Fig. 14(c, d). The divergent responses in the A-DR case due to instability can be again found. In the stable F-DR case, vibrations on the primary are significantly reduced by 94.4% once the active control

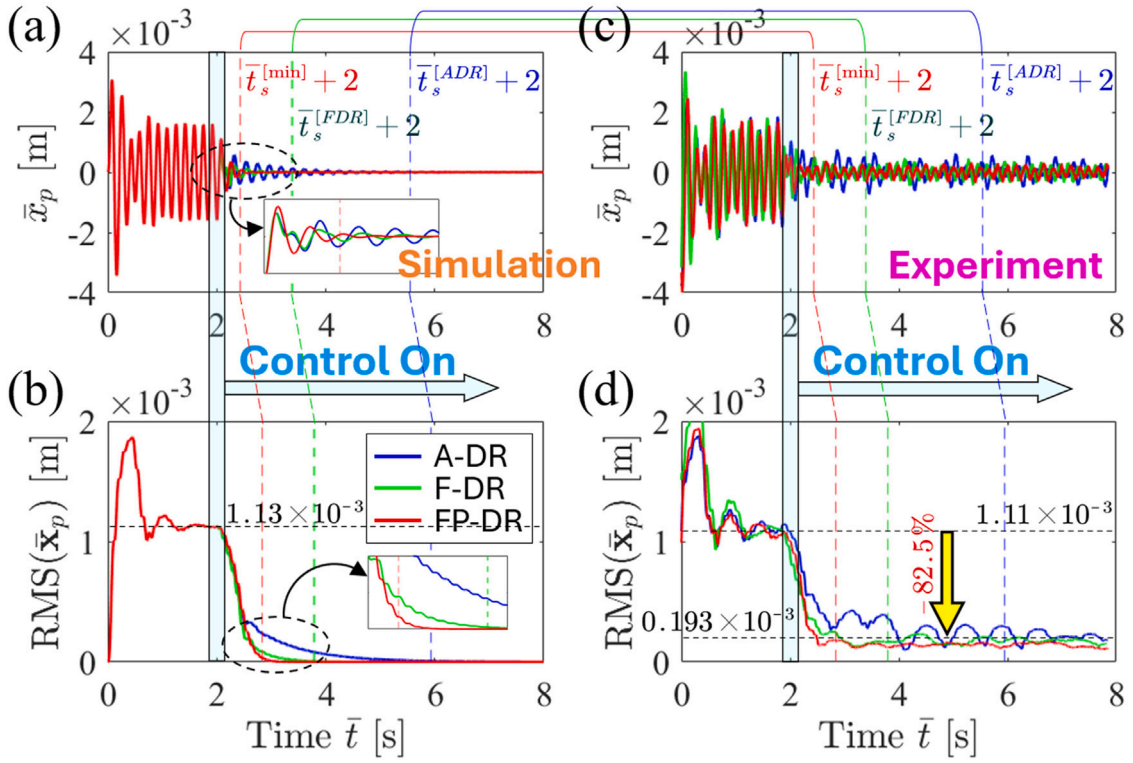


**Fig. 15.** Tests for the transient performances of the A-DR, F-DR, and FP-DR at $\bar{\omega} = 6$ Hz. Tuned pairs are with $\rho_a, \rho_f > 0$ and $b = 1$. Active force $u$ is activated when $\bar{t} \geqslant 2$ s. (a, b). Simulations. (c, d). Experiments. RMS in (b, d) refers to root mean squares for the dataset $\bar{\mathbf{x}}_p$ sampled within the last 0.4 s before the current time step $\bar{t}$.

(pure feedback force) is activated. Possible reasons for small residual vibrations in steady states include noises and inaccurate control parameters due to inaccurate structural parameters, as to be handled by the FP-DR.

### *7.3. Single-frequency case $P = 1$: Expedited transient process*

Based on the theoretical results in Fig. 6, we next combine feedback and feedforward forces to enhance transient performance. To benefit demonstration, the single-frequency excitation at $\bar{\omega} = 6$ Hz is considered. Selecting $\rho_a, \rho_f > 0$ and $b = 1$, we have $\left(\bar{g}_{a.t}^{[1]}, \bar{\tau}_{a.t}^{[1]}\right)$ =(239.17 N/m, 128.1 ms) for the A-DR and $\left(\bar{g}_{f.t}^{[1]}, \bar{\tau}_{f.t}^{[1]}\right)$ =(0.328, 42.0 ms) for the F-DR and FP-DR. Particularly, applying the FP-DR needs to design the feedback force governed by $(g_p, \tau_p)$. We following Fig. 5 adopt $(g_p, \tau_p)$ =(0.266, 3.166) or $(\bar{g}_p, \bar{\tau}_p) = (g_p \bar{k}_p, \tau_p/\bar{\omega}_p)$ = (389.69 N/m, 81.3 ms) to minimize the settling time $\bar{t}_s = t_s/\bar{\omega}_p$ in (42) and thus to expedite the transient process. Comparisons in such A-DR, F-DR, and FP-DR cases are conducted in Fig. 15.

The desired complete vibration suppression in the three cases can be found in the simulation results shown in Fig. 15(a, b). This also verifies that the feedback force of the FP-DR does not affect the tuning mechanism of the feedforward control (i.e., the F-DR). Revisiting Figs. 5 and 6, the dominant roots $s_{dom}$ of the system satisfy $\sigma_{dom}^{[ADR]} = -0.029$, $\sigma_{dom}^{[FDR]} = -0.074$, and $\sigma_{dom}^{[\min]} = -0237$ in the above A-DR, F-DR, and the optimized FP-DR cases, respectively. The corresponding theoretical settling time is then $\bar{t}_s^{[ADR]} = 3.54$ s, $\bar{t}_s^{[\min]} = 1.38$ s, and $\bar{t}_s^{[\min]} = 0.43$ s, as marked in Fig. 15(a). In Fig. 15(b), the settling time is forward-shifted by 0.4 s to compensate for the time for the data collection of the RMS calculation. Clearly, theoretical results well predict the numerical ones. Note that the F-DR expedites the transient process of the A-DR, and the FP-DR can further enhance the transient performance of the F-DR by properly designing the additional feedback control, agreeing with Fig. 6.

The experimental results are shown in Fig. 15(c, d), where the theoretical settling time $\bar{t}_s$ still exhibits sufficient accuracy. Although residual vibrations remain at last, the time to the steady states in the F-DR and the optimized FP-DR cases are much shorter than that in the classical A-DR case, and the system reaches steady states fastest in the FP-DR case, as expected. Compared with Fig. 14(c, d), vibration suppression efficacy in steady states is reduced from 94.4% to 82.5%. One reason is that the current excitation frequency $\bar{\omega} = 6$ Hz is around the natural frequency $\bar{\omega}_a = 6.11$ Hz of the absorber so the given slightly damped absorber can yield sufficient vibration reduction in the passive case $\bar{t} < 2$ s, see also Fig. 7(a). Reducing the residual vibrations needs to improve the steady-state performance, as to be tested next.

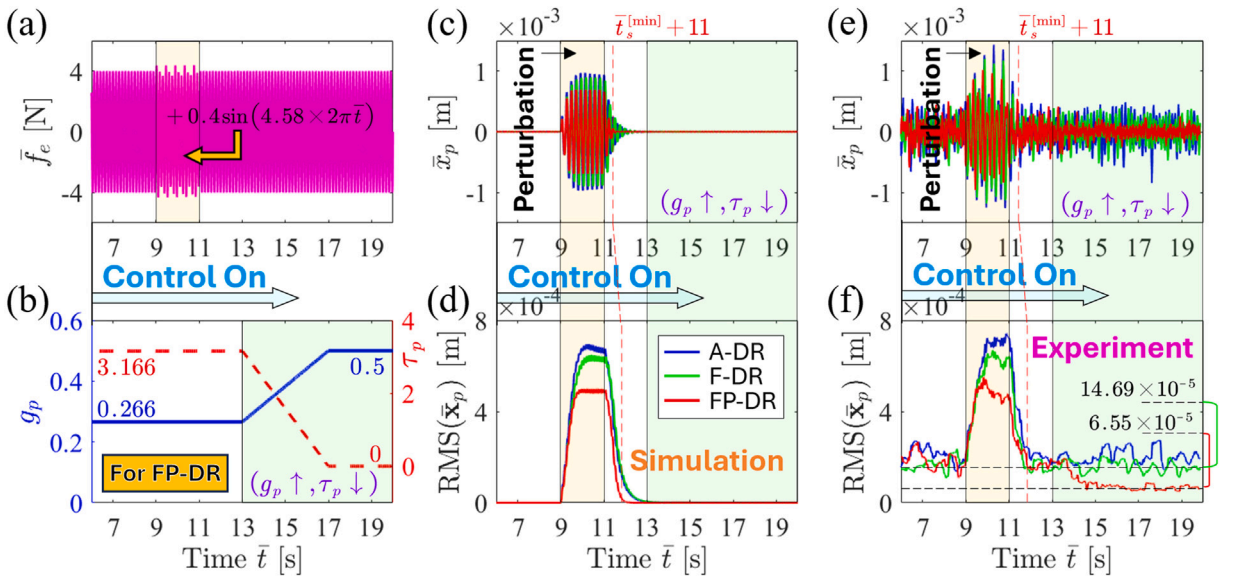


**Fig. 16.** Tests for the steady-state performances of the A-DR, F-DR, and FP-DR at $\bar{\omega} = 6.9$ Hz. Tuned pairs are with $\rho_a, \rho_f > 0$ and $b = 1$. Active force $u$ is activated when $\bar{t} \geqslant 2$ s. (a). Excitation with perturbation around resonance frequency 4.58 Hz introduced when $\bar{t} \in [9\text{ s}, 11\text{ s}]$. (b). Variations of $(g_p, \tau_p)$ for the FP-DR. (c, d). Simulations. (e, f). Experiments. RMS in (d, f) refers to root mean squares for the dataset $\bar{\mathbf{x}}_p$ sampled within the last 0.4 s before the current time step $\bar{t}$.

### 7.4. Single-frequency case $P = 1$: Enhanced performance in steady states

To suppress the residual vibrations in steady states as experimentally observed in Figs. 14(c, d) and 15(c, d), we extend the antiresonance valley to reduce the response sensitivity of the primary, given that the excited main noises should be distributed around the excitation frequency and that the system should have similar responses when structural parameters slightly vary (i.e., when the inaccuracies in control parameters are small). In light of Figs. 7 and 8, the FP-DR can manipulate the frequency response curves of the primary without affecting the zero antiresonance. In addition to extending the antiresonance valley, the FP-DR can control resonance peaks. For verification, we following Fig. 7 consider the case $\bar{\omega} = 6.9$ Hz and introduce a small perturbation at 4.58 Hz, which is around the resonance frequency of the primary, to the excitation $\bar{f}_e$. Fig. 16 details the tests.

The A-DR, F-DR, and FP-DR tuned with $(\rho_a, \rho_f > 0, b = 1)$ or $\left(\bar{g}_{a,t}^{[1]}, \bar{\tau}_{a,t}^{[1]}\right) = (341.85\text{ N/m}, 93.8\text{ ms})$ and $\left(\bar{g}_{f,t}^{[1]}, \bar{\tau}_{f,t}^{[1]}\right) = (0.355, 19.3\text{ ms})$ are considered, and the transient processes $\bar{t} \in [0, 5\text{ s}]$ as Figs. 14 and 15 are omitted to focus on steady states. Fig. 16(a) depicts the perturbated excitation. Fig. 16(b) shows the variations of $(g_p, \tau_p)$ in the FP-DR case, in which $(g_p, \tau_p) = (0.266, 3.166)$ corresponds to the minimum settling time $\bar{t}_s^{[\min]} = 0.43$ s, as aforementioned. Note that $\tau_p = 0$ within $\bar{t} \in [13\text{ s}, 17\text{ s}]$ signifies the delay value set in the controller. The actual output value must be positive due to the inherent loop delay, which, however, should not significantly affect the extended antiresonance valley since the valley width for $g_p > 0$ increases as $\tau_p$ decreases, i.e., $\tau_p = 0$ is not a critical value to achieve the extension, see Fig. 7, as to be tested next.

Simulations are conducted in Fig. 16(c, d), where the F-DR does not raise the resonance peaks in the A-DR case, and the FP-DR can reduce peaks, consistent with Fig. 7. Besides, system responses after perturbation reach steady states fastest in the FP-DR case also at the time cost $\bar{t}_s^{[\min]}$, a direct result of the fact that the spectral distribution in Fig. 5 for the FP-DR is independent of the tuning frequency. When $\bar{t} \in [13\text{ s}, 17\text{ s}]$, we increase $g_p$ and decrease $\tau_p$ to extend the antiresonance valley as per Fig. 7 and Fig. 8, which poses no effect on the complete vibration suppression of the FP-DR, again verifying that $(g_p, \tau_p)$ do not affect the tuning of $\left(\bar{g}_{f,t}^{[1]}, \bar{\tau}_{f,t}^{[1]}\right)$. The corresponding experimental results are shown in Fig. 16(e, f), where the variations of resonance peaks agree with simulations. When $\bar{t} < 13$ s, the F-DR yields smaller residual vibrations than the A-DR and the FP-DR optimized for $\bar{t}_s^{[\min]}$, agreeing with the theoretical width variations of the antiresonance valley in Figs. 7 and 8. When $\bar{t} \in [13\text{ s}, 17\text{ s}]$, the FP-DR gradually reduces residual vibrations as $g_p$ increases and $\tau_p$ decreases thanks to the accordingly extended antiresonance valley, see also Remark 2 for suppressing nonlinear frictions, finally yielding the best performance. The above verifies that properly designing the feedback force $\bar{u}_p$ of the FP-DR can enhance steady-state performance by resisting resonance perturbations and reducing residual vibrations, thus resulting in more complete vibration suppression in practice.

### 7.5. Complete suppression of the dual-frequency vibrations ($P = 2$)

At last, let us examine the complete suppression of multiple-frequency vibrations. Following Section 6, we consider the case with two frequency components $(\bar{\omega}_1, \bar{\omega}_2) = (6.5\text{ Hz}, 8.5\text{ Hz})$. From Figs. 10 and 11, the classical A-DRs are inoperable due to instability,

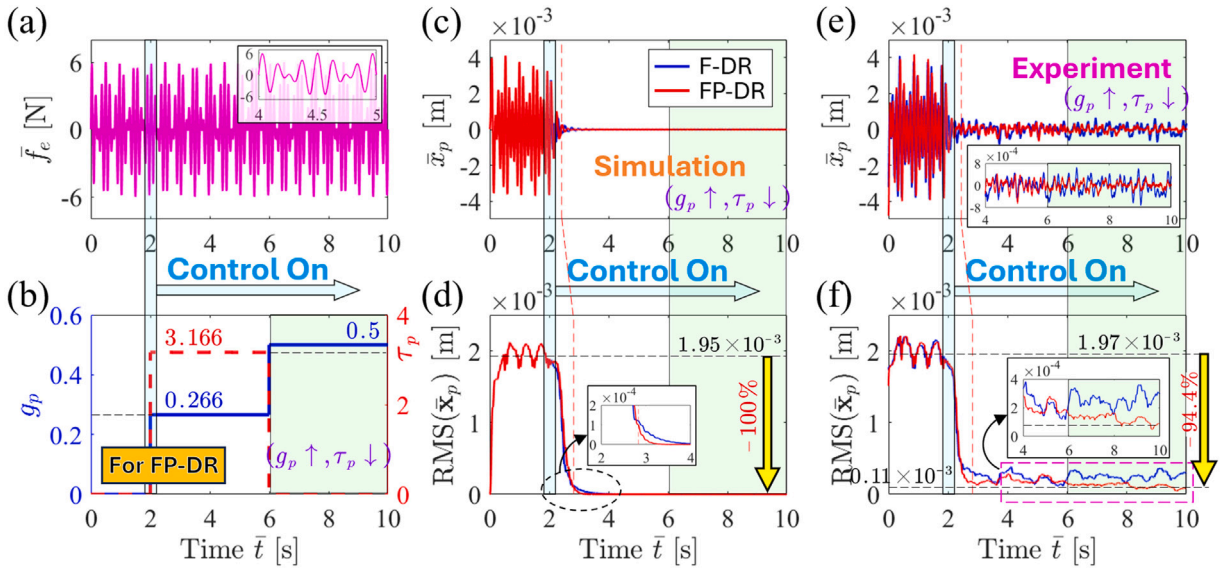


**Fig. 17.** Tests of the F-DR and FP-DR for completely suppressing dual-frequency vibrations with $(\bar{\omega}_1, \bar{\omega}_2) = (6.5\text{ Hz}, 8.5\text{ Hz})$. Control parameters $\left(g_{f,t}^{[1]}, g_{f,t}^{[2]}, \tau_{f,t}^{[1]}, \tau_{f,t}^{[2]}\right)$ are tuned as per (50) with $b = 1$. Active force $u$ is activated when $\bar{t} \geqslant 2$ s. (a). Dual-frequency excitations. (b). Variations of $(g_p, \tau_p)$ for the FP-DR. (c, d). Simulations. (e, f). Experiments. RMS in (d, f) refers to root mean squares for the dataset $\bar{\mathbf{x}}_p$ sampled within the last 0.4 s before the current time step $\bar{t}$.

so we only conduct comparisons between the F-DR and FP-DR. The tuned dimensional control parameters as per (50) for $b = 1$ are $\left(\bar{g}_{f,t}^{[1]}, \bar{g}_{f,t}^{[2]}, \bar{\tau}_{f,t}^{[1]}, \bar{\tau}_{f,t}^{[2]}\right) = (0.805, 0.508, 19.5\text{ ms}, 91.6\text{ ms})$. The tests are detailed in Fig. 17.

Fig. 17(a) shows the time history of the dual-frequency excitation. Fig. 17(b) shows variations of $(g_p, \tau_p)$ when adopting the FP-DR, in which $(g_p, \tau_p) = (0.266, 3.166)$ when $\bar{t} \in [2\text{ s}, 6\text{ s}]$, again aiming to achieve the minimum settling time $\bar{t}_s^{[\min]} = 0.43$ s. To test the extended antiresonance valley by tuning $(g_p, \tau_p)$ as per Fig. 12, we now directly switch $(g_p, \tau_p)$ to $(g_p, \tau_p) = (0.5, 0)$ at $\bar{t} = 6$ s for efficiency as a further step from the modulation process in Fig. 16(b).

The simulations in Fig. 17(c, d) clearly verify that a single delayed vibration absorber following the control logic of the FP-DR can completely suppress multiple-frequency vibrations. Besides, the feedback force governed by $g_p \neq 0$ of the FP-DR also poses no effects on the final complete vibration suppression of the F-DR in the multiple-frequency case, and properly designing $(g_p, \tau_p)$ can expedite the transient process, both of which agree with the theoretical analysis.

The experimental results in Fig. 17(e, f) show that vibrations are significantly suppressed once the active control is introduced. When $\bar{t} \in [2\text{ s}, 6\text{ s}]$, residual vibrations in the cases of the F-DR and the FP-DR optimized for $\bar{t}_s^{[\min]}$ are roughly at the same level. When $\bar{t} > 6$, residual vibrations are reduced by the FP-DR thanks to the extended antiresonance valley as per Fig. 12, finally yielding up to 94.4% vibration reduction compared with the passive case. Particularly, the instantaneous switching of $(g_p, \tau_p)$ at $\bar{t} = 6$ s does not cause notable oscillations compared with the slow modulation process as Fig. 16(b) since the feedback force $\bar{u}_p$ is small when the primary structure is nearly completely settled, i.e., $|\bar{u}| \approx \left|\bar{u}_f\right| \gg \left|\bar{u}_p\right|$. This provides the basis for rapid switching control parameters to expedite suppressing residual vibrations in practice.

## 8. Conclusions

To simplify parametric design and enhance vibration suppression performance of the DR, we propose a hybrid control law consisting of both feedback and feedforward control terms. Particularly, the feedback term is based on the states of the primary and the feedforward one on the excitation force, yielding a new DR called FP-DR. To demonstrate the design rules and to justify the advantages of the FP-DR or the hybrid control law, comparative studies with the classical absorber-based DR (A-DR), which is purely feedback-controlled, and with the F-DR, which is purely feedforward-controlled as the reduced case of the FP-DR, are conducted in the context of both single- and multiple-frequency vibration controls. Main conclusions are as follows.

- Control parameters of the FP-DR that need to be tuned are only related to the feedforward force and are decoupled from system stability which depends only on the feedback force. Compared with the A-DR, whose control parameters affect stability, the determination of the operable control parameters in the FP-DR case becomes very simple.

- The F-DR alone can achieve complete vibration suppression without giving rise to instability. The necessity of using feedforward control to achieve the task is justified by the required much smaller forces than the forces directly applied on the primary to neutralize excitation. The FP-DR modifies the F-DR via the additional feedback forces that take effect only when the primary is not fully settled, forming the basis to enhance complete vibration suppression.
- To guarantee a stable system, the operable control parameters governing the feedback forces of the FP-DR can be analytically obtained independent of the vibration frequency thanks to the decoupling between feedback and feedforward tuning. Furthermore, they can be optimized to expedite the transient process of the F-DR. Such operable and optimum parameters hold regardless of the single- and multiple-frequency cases.
- When suppressing single-frequency vibrations, the tuned pairs of both FP-DR and A-DR are obtained in closed form. The FP-DR and its reduced case, F-DR, extend the operable frequency band of the A-DR, which is bounded by stability issues. In the frequency band where A-DR is operable, the FP-DR can significantly reduce the settling time and extend the antiresonance valley without raising the resonance peaks by tuning the feedback force.
- When suppressing multiple-frequency vibrations, the tuned pairs are available by numerical methods. Two types of A-DRs are considered. One manipulates the pairs of gain and delay. The other doubles the control terms to only manipulate gain parameters while fixing the delay. However, both A-DRs are inoperable due to instability even if each frequency component is operable in the single-frequency case. Alternatively, the FP-DR and F-DR can handle the problem requiring no additional efforts in analyzing system stability and operable control parameters compared with the single-frequency case. Besides, the FP-DR can again enhance the performance of F-DR, thus fully exploiting the strength (raised system order) of the delayed control in suppressing multiple-frequency vibrations by driving a single-mass absorber.

This work applies the feedforward control to the DR for the first time, illustrates the combining strategy with the feedback control, accordingly establishes the basic design and analysis framework, and finally verifies the claimed benefits in suppressing both single- and multiple-frequency vibrations. We believe the FP-DR provides a promising solution in engineering applications of the DR techniques and even the delayed control thanks to the significantly alleviated stability issues of time-delayed systems. Designing prototypes for real uses in automotive will be the next stage of our work.

## CRediT authorship contribution statement

**Yifan Liu:** Writing – review & editing, Writing – original draft, Conceptualization. **Bo Yan:** Writing – review & editing, Funding acquisition. **Jianwang Shao:** Writing – review & editing, Funding acquisition. **Li Cheng:** Writing – review & editing, Supervision, Resources, Project administration.

## Declaration of competing interest

The authors declare that they have no known competing financial interests or personal relationships that could have appeared to influence the work reported in this paper.

## Acknowledgments

This work is supported in part by the National Natural Science Foundation of China (grant nos. 52422504, 52175125, and 51805372) and in part by the National Key R&D Program of China (grant no. 2023YFB2504302).

## Appendix A. Open-source verification materials

The SIMULINK-based simulation models, simulation results, and video recordings of the experiments in Section 7 can be found at https://bit.ly/3QXFHDg.

## Appendix B. Experimental tests on the force output of VCM

This part is to show the definitive relationship between the driving current and the force output of VCM1 to further justify the effectiveness of feedforward control (i.e., the excitation force $\bar{f}_e$ is indeed used to tune $\bar{u}_f$ of the FP-DR and the F-DR as per (24)). An independent test platform is constructed as Fig. 18, where a force sensor is rigidly mounted on the VCM mover, and the VCM stator is fixed on the frame. To improve measurement accuracy, the VCM mover is also fixed on the frame to avoid the inertial effects on the force sensor so the electromagnetic force inside the VCM is statically exerted on the force sensor.

In the test, we introduce a frequency-sweeping current $\bar{I}$ into the VCM mover while fixing the current amplitude $|\bar{I}|$. Particularly, the sweeping rate is sufficiently low as 0.05 Hz/s to suppress transient responses. Two tests under different current amplitudes $|\bar{I}_1| = 0.3$ A and $|\bar{I}_2| = 0.45$ A are performed within $\bar{\omega} \in [4, 10]$ Hz, as detailed in Fig. 19.

Fig. 19(a) and (b) show the reference of the driving current and the force output, respectively. Fig. 19(c) checks the responses of $\bar{f}_e$ at a fixed frequency ($\bar{\omega} = 6$ Hz is considered here as an example), where the agreements between the resulting steady-state amplitudes $(|\bar{f}_{e,1}|, |\bar{f}_{e,2}|)$ and the two in Fig. 19(b) at the corresponding frequency $\bar{\omega} = 6$ Hz indicate that the sweeping ratio is acceptable to settle transient responses. Hence, the envelopes of the results in Fig. 19(b) can be considered as frequency response

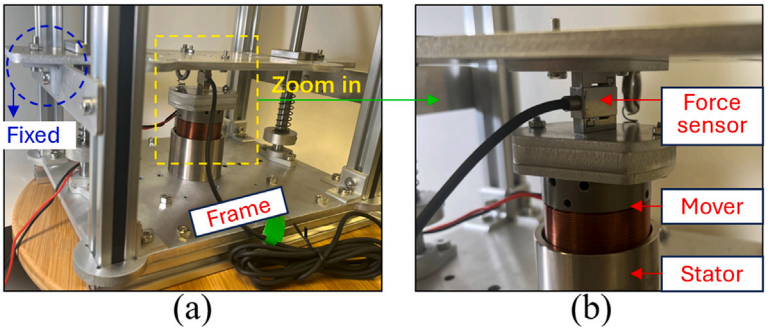


**Fig. 18.** Experimental test platform for examining the relationship between the current input and the force output of the VCM. (a). Overview. (b). Close-up of the force sensor.

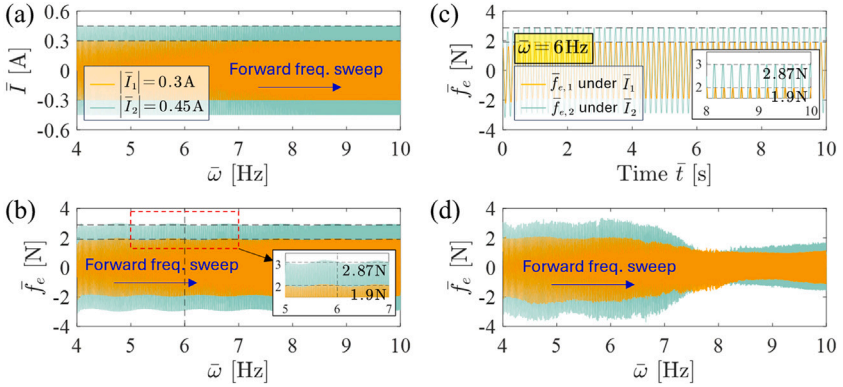


**Fig. 19.** (a). Frequency-sweeping current references for driving VCM. (b). Time history of the statically measured force output. (c). Static force output at a fixed frequency $\bar{\omega} = 6$ Hz. (d). Force output corresponding to (a) when the force sensor is not fixed.

curves of $\bar{f}_e$ under $\bar{I}$. The frequency responses having fixed amplitudes signify the linear relationship between $\bar{f}_e$ and $\bar{I}$ within a sufficiently broad frequency band. Moreover, such a linear relationship can be regarded as constant given that the two tests lead to the same value of $|\bar{f}_{e,1}|/|\bar{I}_1| \approx |\bar{f}_{e,2}|/|\bar{I}_2| \approx \bar{\eta} = 6.36$ N/A, which is known as the thrust constant of the VCM and agrees with the value provided by the VCM manufacturer, i.e., $\bar{\eta}_0 = 6$ N/A with a maximum of 10% tolerance.

Fig. 19(d) shows the measured force when the VCM mover is not fixed, and clearly, the results mismatch the previous static case due to the mentioned inertial effects. Correction methods for measuring dynamical forces are another topic that can be referred to [62–64]. Note that such measurement mismatches lead to deviations of the gain $\bar{g}_f^{[i]}$. However, they should not significantly affect the final performance of the proposed FP-DR since the feedforward control does not affect system stability and since the complete vibration suppression $|\bar{x}_p| = 0$ is equivalent to the static case (see Fig. 1(b)). That is, the uncorrected dynamical forces directly measured by the force sensor deployed as Fig. 18(b) should not affect the expected complete vibration suppression in steady states. Possible consequences are to amplify residual vibrations, which, however, can be beneficially suppressed by the feedback control $\bar{u}_p$. The above observations help simplify the practical implementations of the FP-DR.

**Remark 4.** Direct measurement of the excitation forces is not necessary when deploying the FP-DR in some applications. Fig. 20 shows an example where the excitation is a movable base with displacement $\bar{x}_b$. In this case, one only needs to measure $\bar{x}_b$ or its derivatives $(\dot{\bar{x}}_b, \ddot{\bar{x}}_b)$ for the feedforward states. This problem of reducing the vibration transmission from $\bar{x}_b$ to $\bar{x}_p$ is known as vibration isolation [65–67], which, however, can follow the same analysis procedure in this work given that the primary structure is essentially still force-excited (by the forces provided by $(\bar{k}_p, \bar{c}_p)$ arising from the relative motion $\bar{x}_p - \bar{x}_b$). ■

## Data availability

Data will be made available on request.

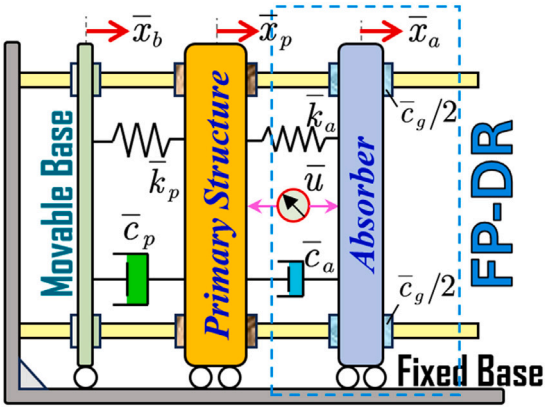


**Fig. 20.** A possible application of the FP-DR to handle displacement-excited vibrations.

## References


[1] N. Olgac, B. Holm-Hansen, A novel active vibration absorption technique: delayed resonator, J. Sound Vib. 176 (1) (1994) 93–104.
[2] H. Elmali, M. Renzulli, N. Olgac, Experimental comparison of delayed resonator and PD controlled vibration absorbers using electromagnetic actuators, J. Dyn. Sys. Meas. Control. 122 (3) (2000) 514–520.
[3] D. Filipovic, N. Olgac, Torsional delayed resonator with velocity feedback, IEEE/ASME Trans. Mechatronics 3 (1) (1998) 67–72.
[4] T. Vyhlídal, N. Olgac, V. Kučera, Delayed resonator with acceleration feedback–complete stability analysis by spectral methods and vibration absorber design, J. Sound Vib. 333 (25) (2014) 6781–6795.
[5] Y. Sun, J. Xu, Experiments and analysis for a controlled mechanical absorber considering delay effect, J. Sound Vib. 339 (2015) 25–37.
[6] J. Xu, Y. Sun, Experimental studies on active control of a dynamic system via a time-delayed absorber, Acta Mech. Sin. 31 (2015) 229–247.
[7] D. Pilbauer, T. Vyhlídal, N. Olgac, Delayed resonator with distributed delay in acceleration feedback—design and experimental verification, IEEE/ASME Trans. Mechatronics 21 (4) (2016) 2120–2131.
[8] V. Kučera, D. Pilbauer, T. Vyhlídal, N. Olgac, Extended delayed resonators–design and experimental verification, Mechatronics 41 (2017) 29–44.
[9] Y. Liu, N. Olgac, L. Cheng, Delayed resonator with multiple distributed delays–considering and optimizing the inherent loop delay, J. Sound Vib. 576 (2024) 118290.
[10] D. Pilbauer, T. Vyhlídal, W. Michiels, Optimized design of robust resonator with distributed time-delay, J. Sound Vib. 443 (2019) 576–590.
[11] M. Kuře, J. Bušek, I. Boussaada, W. Michiels, S.-I. Niculescu, T. Vyhlídal, Robust delayed resonator with acceleration feedback—design by double root assignment and experimental validation, J. Sound Vib. 576 (2024) 118261.
[12] O. Eris, B. Alikoc, A.F. Ergenc, A new delayed resonator design approach for extended operable frequency range, J. Vib. Acoust. 140 (4) (2018) 041003.
[13] T. Vyhlídal, D. Pilbauer, B. Alikoc, W. Michiels, Analysis and design aspects of delayed resonator absorber with position, velocity or acceleration feedback, J. Sound Vib. 459 (2019) 114831.
[14] J. Cai, Q. Gao, Y. Liu, N. Olgac, Control design, analysis, and optimization of fractional-order delayed resonator for complete vibration absorption, J. Sound Vib. 571 (2024) 118083.
[15] J. Cai, Y. Liu, Q. Gao, Y. Chen, Spectrum-based stability analysis for fractional-order delayed resonator with order scheduling, J. Sound Vib. 546 (2023) 117440.
[16] Y. Zhang, C. Ren, K. Ma, Z. Xu, P. Zhou, Y. Chen, Effect of delayed resonator on the vibration reduction performance of vehicle active seat suspension, J. Low Freq. Noise Vib. Act. Control. 41 (1) (2022) 387–404.
[17] K. Wu, C. Ren, Y. Nan, L. Li, S. Yuan, S. Shao, Z. Sun, Experimental research on vehicle active suspension based on time-delay control, Internat. J. Control 97 (5) (2024) 1157–1173.
[18] Y. Liu, L. Cheng, A high-static-low-dynamic-stiffness delayed resonator vibration absorber, Commun. Nonlinear Sci. Numer. Simul. 140 (2025) 108299.
[19] F. Wang, X. Sun, H. Meng, J. Xu, Time-delayed feedback control design and its application for vibration absorption, IEEE Trans. Ind. Electron. 68 (9) (2020) 8593–8602.
[20] X. Zhang, J. Xu, J. Ji, Modelling and tuning for a time-delayed vibration absorber with friction, J. Sound Vib. 424 (2018) 137–157.
[21] Z. Šika, J. Krivošej, T. Vyhlídal, Three dimensional delayed resonator of Stewart platform type for entire absorption of fully spatial vibration, J. Sound Vib. (2024) 118154.
[22] Z. Šika, T. Vyhlídal, Z. Neusser, Two-dimensional delayed resonator for entire vibration absorption, J. Sound Vib. 500 (2021) 116010.
[23] T. Vyhlídal, W. Michiels, Z. Neusser, J. Bušek, Z. Šika, Analysis and optimized design of an actively controlled two-dimensional delayed resonator, Mech. Syst. Signal Process. 178 (2022) 109195.
[24] P. Beneš, J. Gregor, W. Michiels, T. Vyhlídal, Z. Šika, Collocated and non-collocated active spatial absorbers for spatial flexible structures, Mech. Based Des. Struct. Mach. (2024) 1–29.
[25] N. Olgac, R. Jenkins, Actively tuned noncollocated vibration absorption: An unexplored venue in vibration science and a benchmark problem, IEEE Trans. Control Syst. Technol. 29 (1) (2020) 294–304.
[26] A. Saldanha, W. Michiels, M. Kuře, J. Bušek, T. Vyhlídal, Stability optimization of time-delay systems with zero-location constraints applied to non-collocated vibration suppression, Mech. Syst. Signal Process. 208 (2024) 110886.
[27] J. Du, X. Liu, H. Dai, X. Long, Robust combined time delay control for milling chatter suppression of flexible workpieces, Int. J. Mech. Sci. 274 (2024) 109257.
[28] Y. Gao, L. Wang, Broad bandgap active metamaterials with optimal time-delayed control, Int. J. Mech. Sci. 254 (2023) 108449.
[29] M. Karama, M. Hamdi, M. Habbad, Energy harvesting in a nonlinear energy sink absorber using delayed resonators, Nonlinear Dynam. 105 (1) (2021) 113–129.
[30] X. Mao, W. Ding, Nonlinear dynamics and optimization of a vibration reduction system with time delay, Commun. Nonlinear Sci. Numer. Simul. 122 (2023) 107220.

[31] J. Peng, Y. Li, S. Lenci, X. Yang, L. Wang, Vibration suppression of suspended cables with three-to-one internal resonances via time-delay feedback, Eur. J. Mech. A Solids 109 (2025) 105487.
[32] J. Peng, H. Xia, S. Lenci, X. Xie, L. Wang, Nonlinear time-delay feedback control of a suspended cable under temperature effect, Int. J. Non-Linear Mech. 170 (2025) 104975.
[33] X. Sun, J. Xu, J. Fu, The effect and design of time delay in feedback control for a nonlinear isolation system, Mech. Syst. Signal Process. 87 (2017) 206–217.
[34] J.K. Hale, E.F. Infante, F.-S.P. Tsen, Stability in linear delay equations, J. Math. Anal. Appl. 105 (2) (1985) 533–555.
[35] Q. Zhu, J.-Z. Yue, W.-Q. Liu, X.-D. Wang, J. Chen, G.-D. Hu, Active vibration control for piezoelectricity cantilever beam: an adaptive feedforward control method, Smart Mater. Struct. 26 (4) (2017) 047003.
[36] K. Matsui, H. Kajiwara, Feedforward control input generation method for a crane system with restrictions on drive system, Mech. Syst. Signal Process. 170 (2022) 108865.
[37] M.A. Beijen, M.F. Heertjes, H. Butler, M. Steinbuch, Disturbance feedforward control for active vibration isolation systems with internal isolator dynamics, J. Sound Vib. 436 (2018) 220–235.
[38] B. Yan, X. Wang, H. Ma, W. Lu, Q. Li, Hybrid time-delayed feedforward and feedback control of lever-type quasi-zero-stiffness vibration isolators, IEEE Trans. Ind. Electron. 99 (2023) 1–10.
[39] K. Lang, L. Shang, P. Xia, L. Song, An excellent harmonic feedforward-sliding mode output feedback hybrid algorithm for helicopter active vibration control, J. Vib. Control 29 (15–16) (2023) 3528–3543.
[40] W. Zhou, X. Hu, X. Wang, Z. Zhang, T. Zhang, Active compound shape/vibration control of piezo-actuated variable camber wing section via hybrid feedback/feedforward control scheme, Aerosp. Sci. Technol. 151 (2024) 109268.
[41] T.-B. Airimitoaie, I.D. Landau, Combined adaptive feedback and feedforward compensation for active vibration control using Youla–Kučera parametrization, J. Sound Vib. 434 (2018) 422–441.
[42] M.A. Beijen, M.F. Heertjes, H. Butler, M. Steinbuch, Mixed feedback and feedforward control design for multi-axis vibration isolation systems, Mechatronics 61 (2019) 106–116.
[43] L. Dai, X. Li, Y. Zhu, M. Zhang, Auto-tuning of model-based feedforward controller by feedback control signal in ultraprecision motion systems, Mech. Syst. Signal Process. 142 (2020) 106764.
[44] W. Gong, A. Li, J. Ma, P. Wu, F. Qin, An ultra-low frequency vertical isolation system based on composite feedforward and feedback control, IEEE Sensors J. (2023).
[45] Y. Liu, B. Yan, L. Cheng, Delayed resonator with hybrid multiple-delayed control for enhanced complete vibration suppression, IEEE/ASME Trans. Mechatronics (2025) 1–12.
[46] Y. Liu, B. Yan, L. Cheng, H ∞ optimization of a hybrid multiple-delayed delayed resonator vibration absorber, Int. J. Mech. Sci. 300 (2025) 110381.
[47] N. Olgac, H. Elmali, S. Vijayan, Introduction to the dual frequency fixed delayed resonator, J. Sound Vib. 189 (3) (1996) 355–367.
[48] M. Valášek, N. Olgac, Z. Neusser, Real-time tunable single-degree of freedom, multiple-frequency vibration absorber, Mech. Syst. Signal Process. 133 (2019) 106244.
[49] R. Wang, X. Yin, Q. Wang, L. Jiang, Direct amplitude control for voice coil motor on high frequency reciprocating rig, IEEE/ASME Trans. Mechatronics 25 (3) (2020) 1299–1309.
[50] J. Cai, Q. Gao, S. Zhu, Experimental investigation of time-delayed control for enhanced performance in a high-static-low-dynamic-stiffness vibration isolation system, IEEE/ASME Trans. Mechatronics (2024).
[51] Y.-D. Chen, C.-C. Fuh, P.-C. Tung, Application of voice coil motors in active dynamic vibration absorbers, IEEE Trans. Magn. 41 (3) (2005) 1149–1154.
[52] S.M.R. Rasid, T. Mizuno, Y. Ishino, M. Takasaki, M. Hara, D. Yamaguchi, Design and control of active vibration isolation system with an active dynamic vibration absorber operating as accelerometer, J. Sound Vib. 438 (2019) 175–190.
[53] V.B. Kolmanovskii, V.R. Nosov, Stability of Functional Differential Equations, vol. 180, Elsevier, 1986.
[54] N. Olgac, R. Sipahi, An exact method for the stability analysis of time-delayed linear time-invariant (LTI) systems, IEEE Trans. Autom. Control 47 (5) (2002) 793–797.
[55] J. Cai, Q. Gao, Y. Liu, A. Wu, Generalized dixon resultant for strong delay-independent stability of linear systems with multiple delays, IEEE Trans. Autom. Control 69 (4) (2023) 2697–2704.
[56] I.I. Delice, R. Sipahi, Delay-independent stability test for systems with multiple time-delays, IEEE Trans. Autom. Control 57 (4) (2011) 963–972.
[57] R. Lewis, B. Anderson, Necessary and sufficient conditions for delay-independent stability of linear autonomous systems, IEEE Trans. Autom. Control 25 (4) (1980) 735–739.
[58] T. Vyhlidal, P. Zitek, Mapping based algorithm for large-scale computation of Quasi-Polynomial zeros, IEEE Trans. Autom. Control 54 (1) (2009) 171–177.
[59] J.E. Brock, A note on the damped vibration absorber, Trans. ASME, J. Appl. Mech. 13–4 (1946) A–284.
[60] Y. Liu, L. Cheng, Exact h ∞ optimization of dynamic vibration absorbers: Univariate-polynomial-based algorithm and operability analysis, Appl. Math. Model. 139 (2025) 115812.
[61] F. Li, H. Wu, L. Liu, Y. Ye, Y. Wang, P. Wu, Nonlinear optimal frequency control for dynamic vibration absorber and its application, Mech. Syst. Signal Process. 223 (2025) 111932.
[62] M. Ammar, M.I. Mohamed, G.M. Mahmoud, S.R. Hassan, R. Kumme, H. Zakaria, A. Gaafer, A comparison between static and dynamic stiffness of force transducers for dynamic force calibrations, Measurement 203 (2022) 111945.
[63] L.R. Castro, P. Viéville, P. Lipinski, Correction of dynamic effects on force measurements made with piezoelectric dynamometers, Int. J. Mach. Tools Manuf. 46 (14) (2006) 1707–1715.
[64] Y. Fujii, Toward dynamic force calibration, Measurement 42 (7) (2009) 1039–1044.
[65] C. Liu, X. Jing, S. Daley, F. Li, Recent advances in micro-vibration isolation, Mech. Syst. Signal Process. 56 (2015) 55–80.
[66] B. Yan, S. Wang, P. Ling, Z. Yang, H. Ma, Q. Li, Seahorse-exoskeleton-inspired structure with linear-to-torsion transition property for low-frequency vibration isolation, Fundam. Res. (2025).
[67] G. Yan, H.-X. Zou, S. Wang, L.-C. Zhao, Z.-Y. Wu, W.-M. Zhang, Bio-inspired vibration isolation: methodology and design, Appl. Mech. Rev. 73 (2) (2021) 020801.